

Supporting Information for

Green-Solvent Processed Blade-Coating Organic Solar Cells with an Efficiency Approaching 19% Enabled by Alkyl-Tailored Acceptors

Hairui Bai¹, Ruijie Ma^{4, *}, Wenyan Su^{5, 9, *}, Top Archie Dela Peña^{6, 7}, Tengfei Li¹, Lingxiao Tang¹, Jie Yang⁸ Bin Hu¹⁰, Yilin Wang¹, Zhaozhao Bi¹, Yueling Su⁹, Qi Wei⁶, Qiang Wu^{1, *}, Yuwei Duan⁹, Yuxiang Li⁵, Jiaying Wu⁷, Zicheng Ding⁹, Xunfan Liao³, Yinjuan Huang¹, Chao Gao¹¹, Guanghao Lu¹⁰, Mingjie Li⁶, Weiguo Zhu², Gang Li^{4, *}, Qunping Fan^{1, 2, 3, *}, and Wei Ma^{1, *}

¹ State Key Laboratory for Mechanical Behavior of Materials, Xi'an Jiaotong University, Xi'an 710049, P. R. China

² Jiangsu Engineering Research Center of Light-Electricity-Heat Energy-Converting Materials and Applications, School of Materials Science and Engineering, and Changzhou University, Changzhou 213164, P. R. China

³ Key Lab of Fluorine and Silicon for Energy Materials and Chemistry of Ministry of Education/National Engineering Research Center for Carbohydrate Synthesis, Jiangxi Normal University, 99 Ziyang Avenue, Nanchang 330022, P. R. China

⁴ Department of Electronic and Information Engineering, Research Institute for Smart Energy (RISE), The Hong Kong Polytechnic University, Kowloon 999077, Hong Kong, P. R. China

⁵ School of Materials Science and Engineering, Xi'an University of Science and Technology, Xi'an 710054, P. R. China

⁶ Department of Applied Physics, The Hong Kong Polytechnic University, Kowloon, Hong Kong 999077, P. R. China

⁷ Advanced Materials Thrust, Function Hub, The Hong Kong University of Science and Technology, Nansha, Guangzhou, P. R. China

⁸ School of Chemistry and Chemical Engineering, Beijing Institute of Technology, Beijing 100081, P. R. China

⁹ Key Laboratory of Applied Surface and Colloid Chemistry, Ministry of Education, Shaanxi Key Laboratory for Advanced Energy Devices, Shaanxi Engineering Lab for Advanced Energy Technology School of Materials Science and Engineering, Shaanxi Normal University, Xi'an 710119, P. R. China

¹⁰ Frontier Institute of Science and Technology, Xi'an Jiaotong University, Xi'an 710054, P. R. China

¹¹ Xi'an Key Laboratory of Liquid Crystal and Organic Photovoltaic Materials, State Key Laboratory of Fluorine & Nitrogen Chemicals, Xi'an Modern Chemistry Research Institute, Xi'an 710065, P. R. China

*Corresponding authors. E-mail: ruijie.ma@polyu.edu.hk (Ruijie Ma); suwy1027@xust.edu.cn (Wenyan Su); wuqiang@xjtu.edu.cn (Qiang Wu); gang.w.li@polyu.edu.hk (Gang Li); qunping@xjtu.edu.cn (Qunping Fan); msewma@xjtu.edu.cn (Wei Ma)

S1 Experimental Section

Materials: Monomers YBO-CHO [S1], BPSe [S2], and YDT-CHO[S3], Y-series small-molecule acceptor (Y-SMA) L8-BO[S4], polymer donor PM6 with a Mn of 31.7 kDa (Lot# YMA08A in Solarmer Materials Inc) [S5], and end-group NpIC-2F [S6] were synthesized according to the previous reports. YR-SeNF series (YBO-SeNF, YHD-SeNF, and YDT-SeNF) were developed according to the following procedures:

YBO-SeNF: In a dry 100 mL flask, compounds of YBO-2CHO (0.10 g, 0.081 mmol), NpIC-2F (0.080 g, 0.284 mmol), and pyridine (0.1 mL) were added to 10 mL of degassed chloroform under argon and stirred vigorously at 65 °C for 12 h. Then the mixture was poured into methanol (100 mL) followed by precipitation, and the sediments were collected. The resulting crude compound was purified by column chromatography on silica gel with hexane/CH₂Cl₂ (v/v=2:1) as eluent and then it was furtherly purified by crystallized two times using a mix solvent of chloroform/acetone (v/v=1:1) to give YBO-SeNF as a black solid (0.097 g, 68%). ¹H NMR (600 MHz, CDCl₃, TMS), (ppm): δ 9.31 (s, 2H), 9.02 (s, 2H), 8.31 (s, 2H), 7.83-7.77 (m, 4H), 4.76 (t, J = 3.0 Hz, 4H), 3.23 (m, 4H), 2.25-2.22 (m, 2H), 1.86 (m, 4H), 1.55-1.47 (m, 4H), 1.35 (m, 4H), 1.26 (m, 24H), 1.20-1.09 (m, 8H), 1.09-0.91 (m, 12H), 0.85 (m, 12H), 0.76-0.65 (m, 18H). ¹³C NMR (600 MHz, CDCl₃, TMS), (ppm): δ 188.54, 159.94, 157.01, 147.78, 147.47, 142.17, 138.37, 138.18, 135.25, 134.92, 134.26, 133.47, 133.42, 132.47, 132.42, 130.09, 125.48, 122.30, 121.28, 116.56, 116.45, 116.09, 115.98, 115.70, 115.43, 113.71, 66.92, 55.82, 39.03, 31.92, 31.63, 31.58, 31.36, 30.47, 30.36, 29.97, 29.68, 29.64, 29.54, 29.47, 29.41, 29.35, 28.04, 27.92, 25.52, 25.39, 22.89, 22.83, 22.69, 22.53, 22.51, 14.13, 14.07, 14.03, 13.82, 13.79. MALDI-TOF-MS m/z: [M+Na]⁺ calcd. for C₉₈H₁₀₆F₄N₈O₂S₃Se₂Na⁺, 1758.58674+Na⁺, found 1781.58603.

BPSe-HD: In a dry 100 mL flask, compounds of BPSe (0.85 g, 1.01 mmol), K₂CO₃ (1.40 g, 10.1 mmol), KI (3.35 g, 20.2 mmol), and 1-bromo-2-hexyl-decane (1.85 g, 6.06 mmol) were added to 10 mL of degassed DMF under argon and stirred vigorously at 100 °C for 12 h. The reaction was quenched by water and extracted with CH₂Cl₂. The combined extracts were washed with brine, dried over anhydrous MgSO₄, and then filtered and collected solvent. The solvent was removed by rotary evaporation to give the crude product as an orange oil, which was further purified by column chromatography on silica gel with hexane/CH₂Cl₂ (v/v, 8:1) as eluent to afford BPSe-HD as an orange viscous liquid (0.80 g, 61.4%). ¹H NMR (600 MHz, CDCl₃, TMS), (ppm): δ 7.53 (s, 2H), 4.55 (d, J = 7.6 Hz, 4H), 2.85-2.72 (m, 4H), 2.16-1.98 (m, 2H), 1.95-1.75 (m, 4H), 1.45-1.27 (m, 34H), 1.20-0.79 (m, 44H), 0.69-0.65 (m, 18H).

YHD-CHO: In an ice bath, phosphorus oxychloride (POCl₃, 3 mL) was dropwise added into a solution of anhydrous DMF (3 mL) and kept 10 minutes under the protection of argon, and then kept additional 2 hours at room temperature under stirring. After that, BPSe-HD (0.40 g, 0.31 mmol) dissolved in chloroform (10 mL) was added into the reaction mixture and then heated at 65 °C for overnight, cooled to room temperature, quenched with saturated aqueous solution of sodium acetate, and extracted with CH₂Cl₂. The combined extracts were washed with brine, dried over anhydrous MgSO₄, and then filtered and collected solvent. The solvent was removed by rotary evaporation to yield the crude product, which was then purified by column chromatography on silica gel with hexane/CH₂Cl₂ (v/v, 2:1) as eluent to afford YHD-CHO as a red viscous liquid (0.36 g, 86%). ¹H NMR (600 MHz, CDCl₃, TMS), (ppm): δ 10.04 (s, 2H), 4.58 (d, J = 7.6 Hz, 4H), 3.18 (t, J = 7.6 Hz, 4H), 2.09-1.98 (m, 2H), 1.98-1.83 (m, 4H), 1.51-1.26 (m, 34H), 1.19-0.79 (m, 44H), 0.69-0.65 (m, 18H).

YHD-SeNF: In a dry 100 mL flask, compounds of YHD-2CHO (0.090 g, 0.067 mmol), NpIC-2F (0.067 g, 0.234 mmol), and pyridine (0.1 mL) were added to 10 mL of degassed chloroform under argon and stirred vigorously at 65 °C for 12 h. Then the mixture was poured

into methanol (100 mL) followed by precipitation, and the sediments were collected. The resulting crude compound was purified by column chromatography on silica gel with hexane/CH₂Cl₂ ($v/v=2:1$) as eluent and then it was furtherly purified by crystallized two times using a mix solvent of chloroform/acetone ($v/v=1:1$) to give YHD-SeNF as a black solid (0.089 g, 71%). ¹H NMR (600 MHz, CDCl₃, TMS), (ppm): δ 9.30 (s, 2H), 9.01 (s, 2H), 8.31 (s, 2H), 7.83-7.75 (m, 4H), 4.77 (d, $J = 7.3$ Hz, 4H), 3.22 (t, $J = 7.5$ Hz, 4H), 2.35-2.15 (m, 2H), 1.97-1.73 (m, 4H), 1.54-1.25 (m, 34H), 1.19-1.03 (m, 40), 0.88-0.71 (m, 22H). ¹³C NMR (600 MHz, CDCl₃, TMS), (ppm): δ 188.48, 159.63, 156.94, 147.88, 147.38, 142.27, 138.60, 137.99, 135.19, 134.98, 134.25, 133.47, 133.39, 132.53, 132.44, 130.02, 125.38, 123.30, 121.10, 116.53, 116.37, 116.22, 116.05, 115.75, 115.45, 113.84, 66.86, 55.99, 39.24, 32.00, 31.96, 31.73, 31.44, 30.77, 30.10, 30.00, 29.79, 29.73, 29.67, 29.51, 29.45, 29.35, 25.89, 25.82, 22.77, 22.75, 22.66, 14.24, 14.21. MALDI-TOF-MS m/z: [M]⁺ calcd. for C₁₀₆H₁₂₂F₄N₈O₂S₃Se₂, 1871.71530, found 1871.72891.

YDT-SeNF: In a dry 100 mL flask, compounds of YDT-2CHO (0.080 g, 0.051 mmol), NpIC-2F (0.050 g, 0.178 mmol), and pyridine (0.1 mL) were added to 10 mL of degassed chloroform under argon and stirred vigorously at 65 °C for 12 h. Then the mixture was poured into methanol (100 mL) followed by precipitation, and the sediments were collected. The resulting crude compound was purified by column chromatography on silica gel with hexane/CH₂Cl₂ ($v/v=2:1$) as eluent and then it was furtherly purified by crystallized two times using a mix solvent of chloroform/acetone ($v/v=1:1$) to give YDT-SeNF as a black solid (0.078 g, 73%). ¹H NMR (600 MHz, CDCl₃, TMS), (ppm): δ 9.31 (s, 2H), 9.03 (s, 2H), 8.31 (s, 2H), 7.83-7.75 (m, 4H), 4.76 (d, $J = 7.0$ Hz, 4H), 3.22 (t, $J = 7.4$ Hz, 4H), 2.39-2.16 (m, 2H), 1.98-1.76 (m, 4H), 1.55-1.02 (m, 98H), 0.88-0.79 (m, 22H). ¹³C NMR (600 MHz, CDCl₃, TMS), (ppm): δ 188.54, 159.85, 157.03, 147.86, 147.51, 142.25, 138.54, 138.13, 135.28, 135.02, 134.36, 133.54, 133.46, 132.53, 132.46, 130.17, 125.51, 123.31, 121.24, 116.66, 116.46, 116.17, 115.99, 115.74, 115.48, 113.82, 66.92, 55.86, 39.08, 32.05, 32.03, 31.75, 31.45, 30.62, 30.12, 29.92, 29.84, 29.75, 29.69, 29.57, 29.51, 29.47, 25.76, 25.73, 22.79, 14.21. MALDI-TOF-MS m/z: [M+Na]⁺ calcd. for C₁₂₂H₁₅₄F₄N₈O₂S₃Se₂Na⁺, 2095.96570+Na⁺, found 2117.95845.

Instruments and Measurements: ¹H NMR and ¹³C NMR spectra were collected with a Bruker 600 MHz ASCEND ADVANCE III HD spectrometer in CDCl₃. The UV-vis absorption spectra were measured by a Shimadzu UV-3600 Plus Spectrophotometer. Cyclic voltammetry was probed on a CHI660D electrochemical workstation in an anhydrous acetonitrile solution of tetra-n-butylammonium hexafluoro-phosphate (Bu₄NPF₆) (0.1 M) with a scan rate of 50 mV s⁻¹. A conventional three-electrode cell was used with a platinum plate working electrode, a platinum wire counter-electrode, and an Ag/AgCl reference electrode. Ferrocene/Ferrocenium (Fc/Fc⁺) used as the internal standard and their energy levels are assumed at -4.8 eV relative to vacuum. The corresponding HOMO and LUMO levels are estimated according to the empirical equations: E_{HOMO}= -(E_{ox}+4.28) eV and E_{LUMO}= -(E_{red}+4.28) eV. Atomic force microscopy (AFM) characterization was scanned by Veeco INNOVA Atomic Force Microscope using a tapping mode. Transmission electron microscopy (TEM) was performed using a Tecnai G2 F20 S-TWIN instrument at 200 kV accelerating voltage. TEM was performed using a Tecnai G2 F20 S-TWIN instrument at 200 kV accelerating voltage, in which the blend films were prepared using a processing technique, as following: first, the blend films were blade-coating on the PEDOT:PSS/ITO substrates; second, the resulting blend film/PEDOT:PSS/ITO substrates were submerged in deionized water to make these blend films float onto the air-water interface; finally, the floated blend films were taken up on unsupported 200 mesh copper grids for a TEM measurement. GIWAXS measurements were performed at beamline 7.3.3 at the Advanced Light Source.

Samples were prepared on Si substrates using identical blend solutions as those used in devices. The 10 keV X-ray beam was incident at a grazing angle of 0.11-0.15°, selected to maximize the scattering intensity from the samples. The scattered x-rays were detected using a Dectris Pilatus 2M photon counting detector. The crystal coherence length (CCL) was defined as $CCL = 0.9 \times (2\pi/\text{FWHM}) (\text{\AA})$, where FWHM is the full width at half maximum of the corresponding diffraction peak.

Computational Details: To gain a deeper understanding of the effect of alkyl-chain engineering on intermolecular interactions and packing patterns, the crystal structures of the studied acceptors were predicted by carrying out molecular dynamics (MD) simulations. Firstly, the single molecule was optimized using the Dmol3 program with a fine accuracy setting. Additionally, electrostatic potential and population analysis were performed. Subsequently, crystal structure prediction was carried out using the Perdew-Burke-Ernzerhof (PBE) exchange-correlation energy functional and the Dreiding force field. This process was conducted in the polymorph module, which has proven to be a valuable method for predicting crystal structures.^[S7] All calculations were performed using Materials Studio (One Molecular Simulation Software, <https://www.accelrys.com>).

Mobility Measurement: The electron and hole mobilities of blends were measured by using a space-charge limited current (SCLC) method. The electron-only device with a structure of ITO/ZnO/active layer/PFN-Br-MA/Ag and the hole-only device with an architecture of ITO/2PACz/active layer/MoO_x/Al were fabricated. The mobility was determined by fitting the dark current to the model of a single carrier SCLC, described by the equation: $J = 9\epsilon_0\epsilon_r\mu V^2/8L^3$, where J is the current density, ϵ_0 is the permittivity of free space, ϵ_r is the relative dielectric constant of the transport medium, μ is the charge mobility and L is the thickness of the active layer. $V = V_{\text{app}} - V_{\text{bi}}$, where V_{app} is the applied voltage, V_{bi} is the offset voltage (V_{bi} is 0 V here). The electron mobility can be calculated from the slope of the $J_{0.5} \sim V$ curves.

Transient Absorption Spectroscopy (TAS): TAS was measured with an amplified Ti:sapphire femtosecond laser (800 nm wavelength, 50 fs, 1 kHz repetition; Coherent Libra) and a Helios pump/probe setup (Ultrafast Systems). The 400 nm pump pulses with a pump fluence of 0.5 or < 0.3 μJ/cm² were obtained by frequency doubling the 800 nm fundamental regenerative amplifier output. The white-light continuum probe pulses were generated by focusing a small portion of the regenerative amplifier's fundamental 800 nm laser pulses into a 2 mm sapphire crystal.

S2 Supplementary Figures and Tables

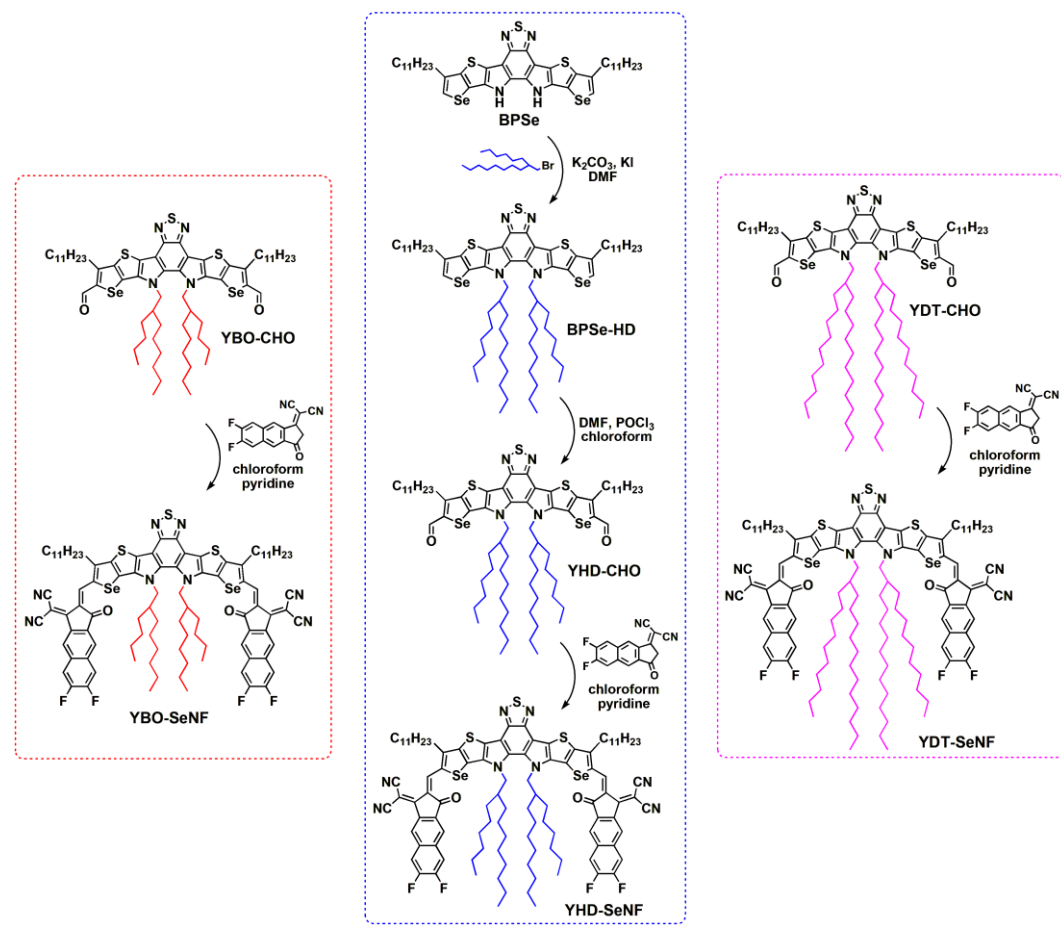


Fig. S1 The synthetic routes of YBO-SeNF, YHD-SeNF, and YDT-SeNF

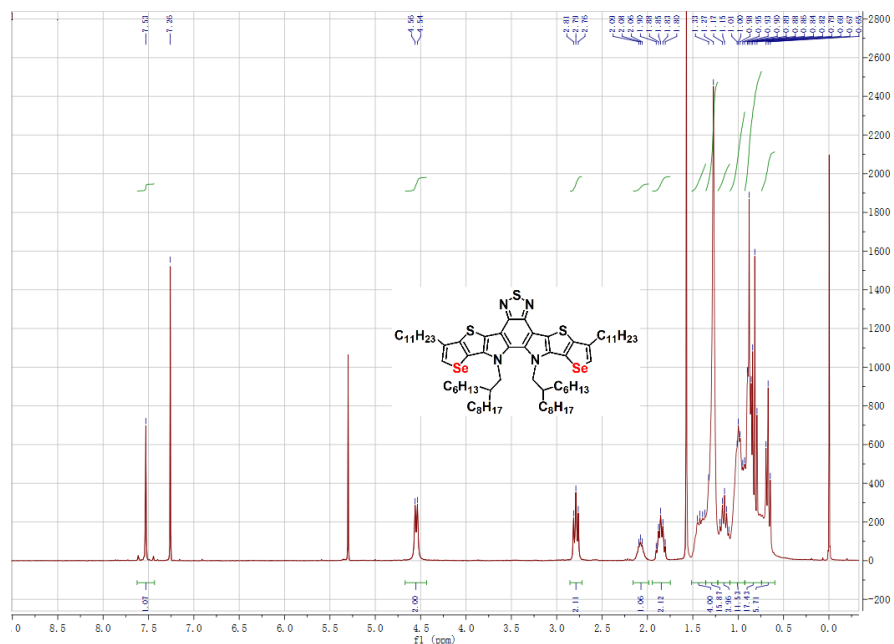


Fig. S2 ¹H NMR image of BPSe-HD

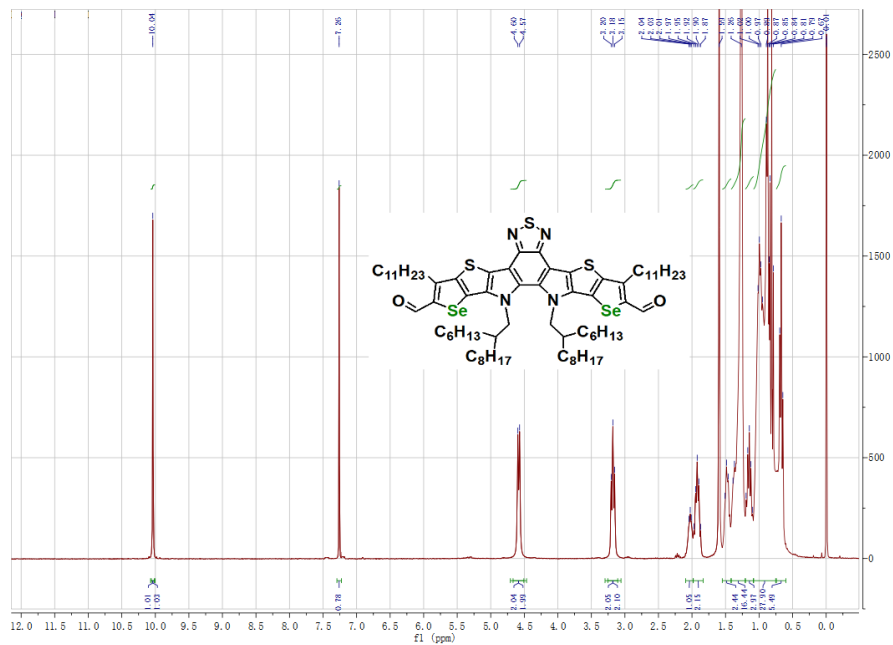


Fig. S3 ¹H NMR image of YHD-CHO

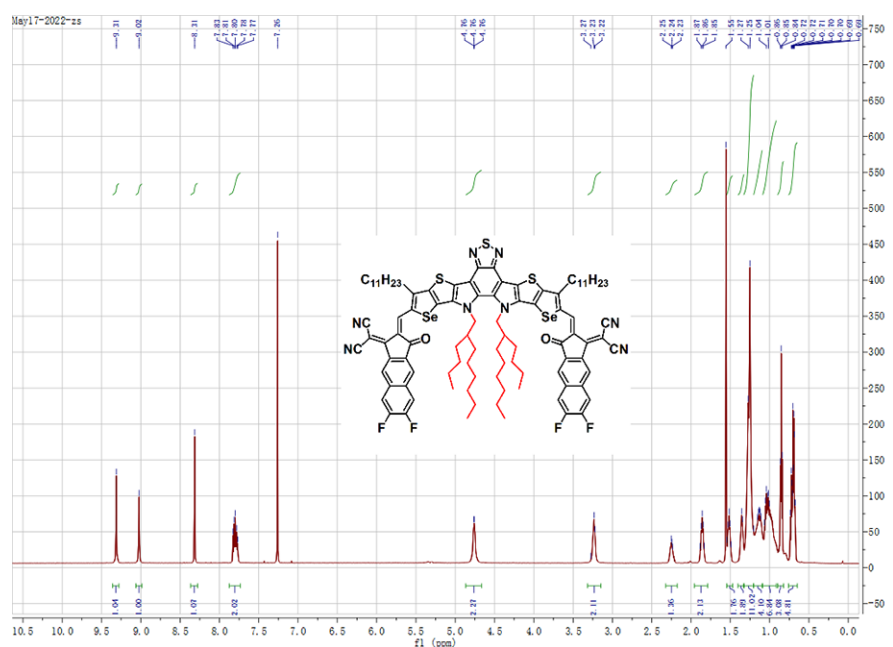


Fig. S4 ¹H NMR image of YBO-SeNF

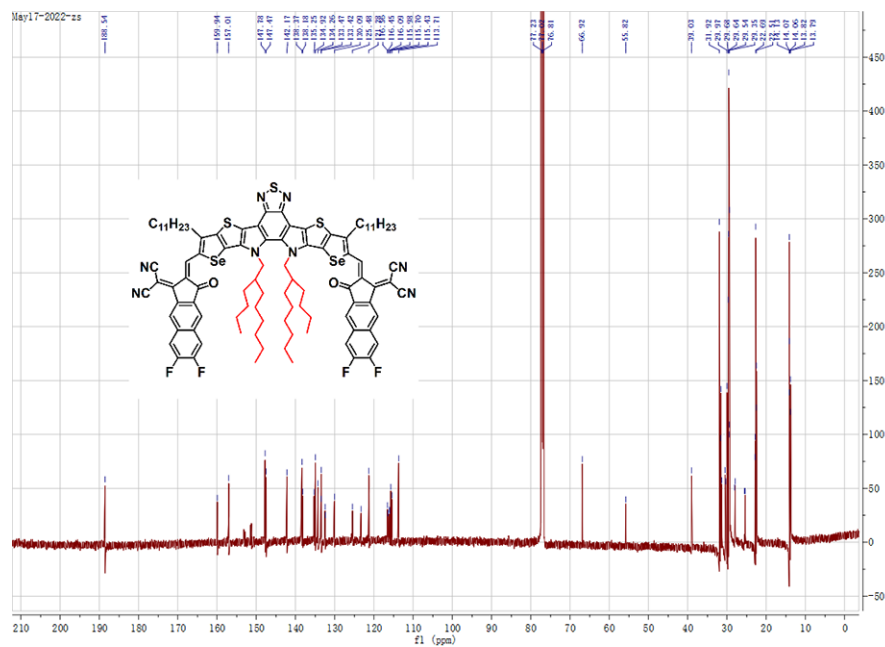


Fig. S5 ^{13}C NMR image of YBO-SeNF

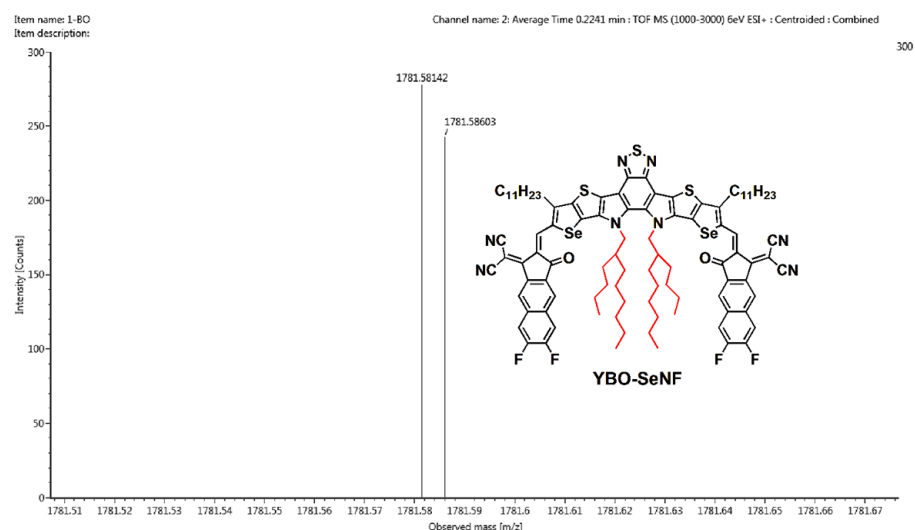


Fig. S6 MS image of YBO-SeNF

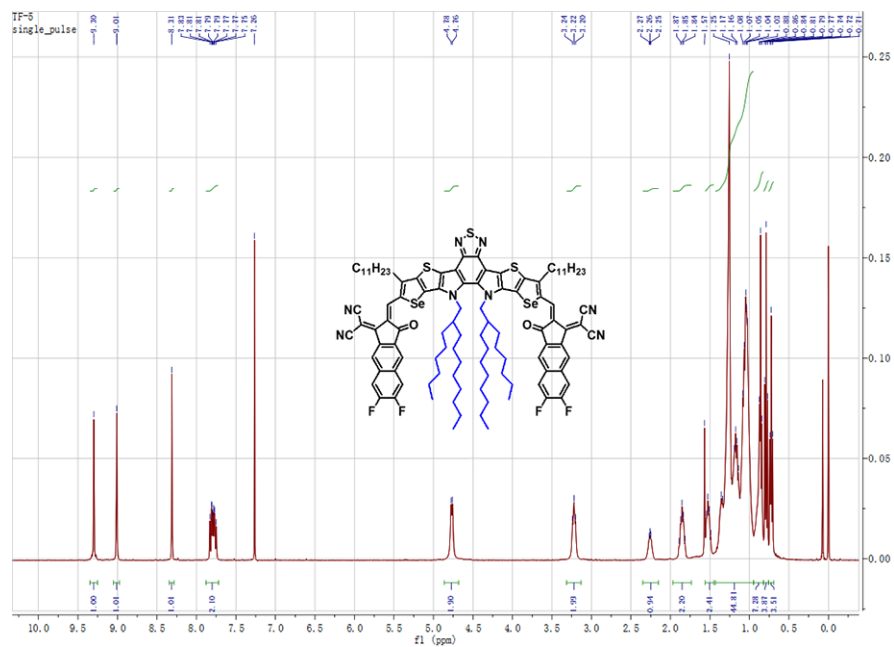


Fig. S7 ^1H NMR image of YHD-SeNF

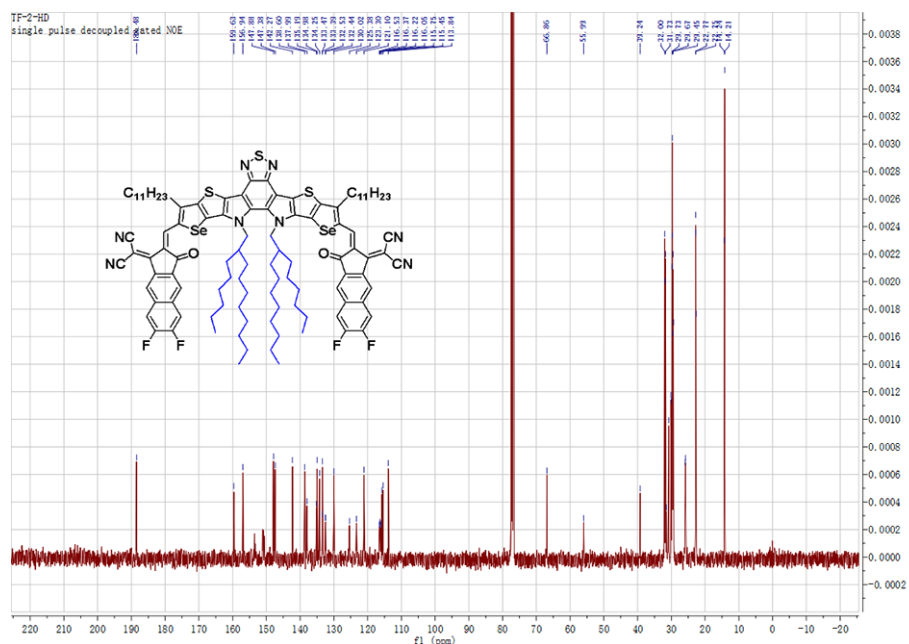


Fig. S8 ^{13}C NMR image of YHD-SeNF

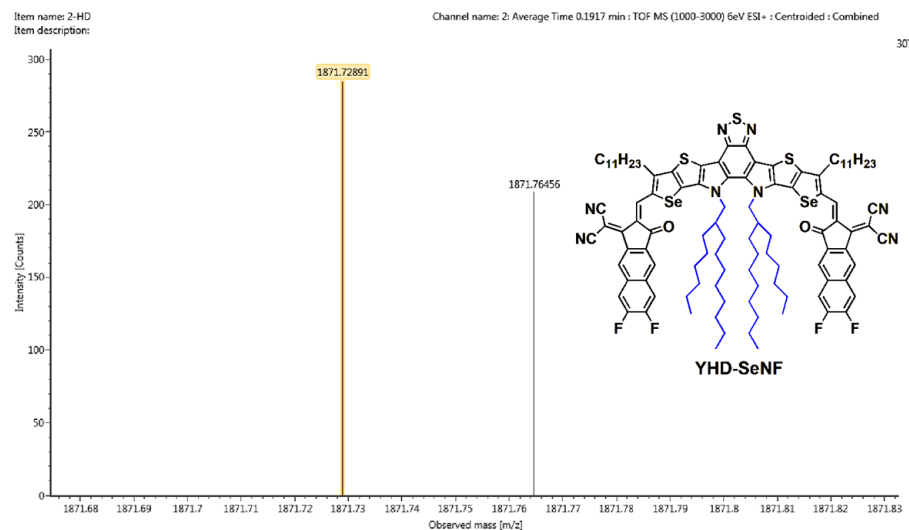


Fig. S9 MS image of YHD-SeNF

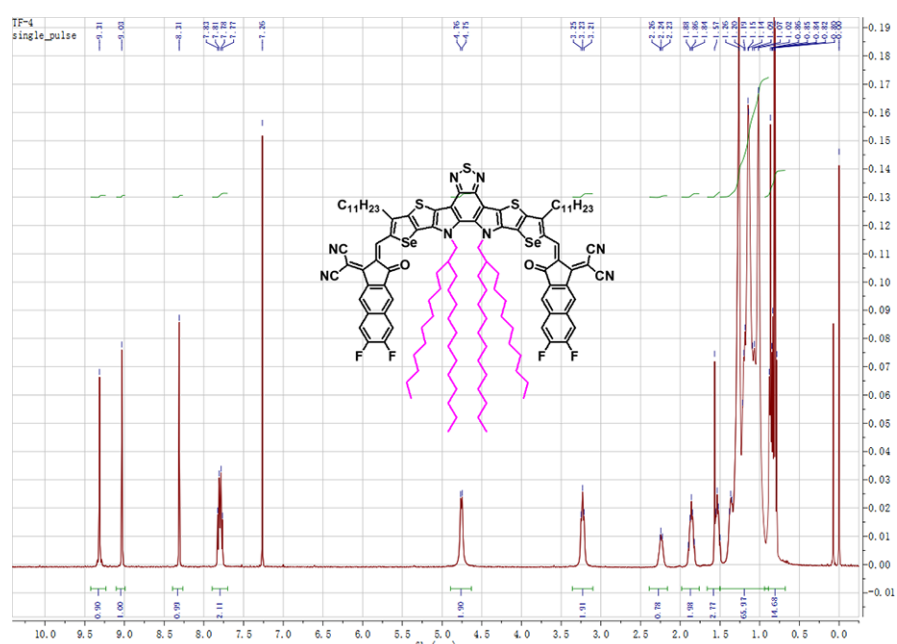


Fig. S10 ^1H NMR image of YDT-SeNF

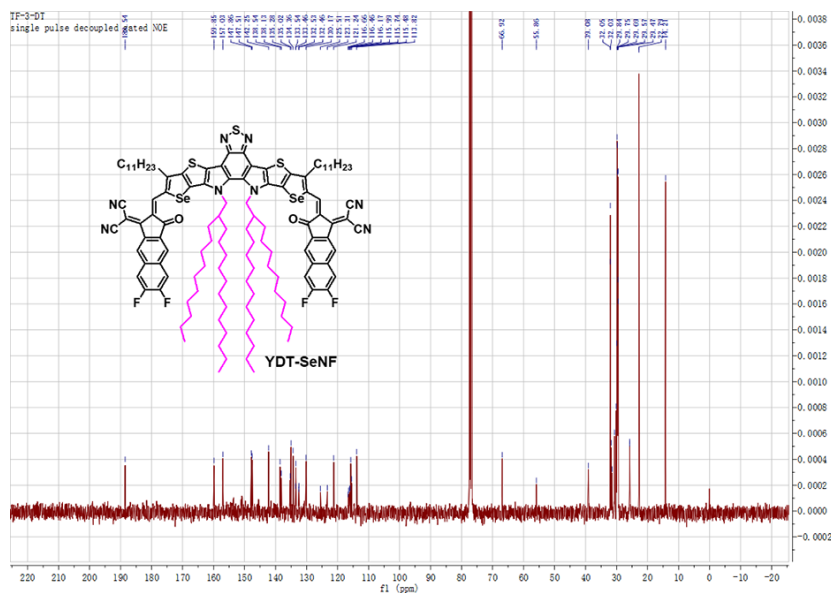


Fig. S11 ¹³C NMR image of YDT-SeNF

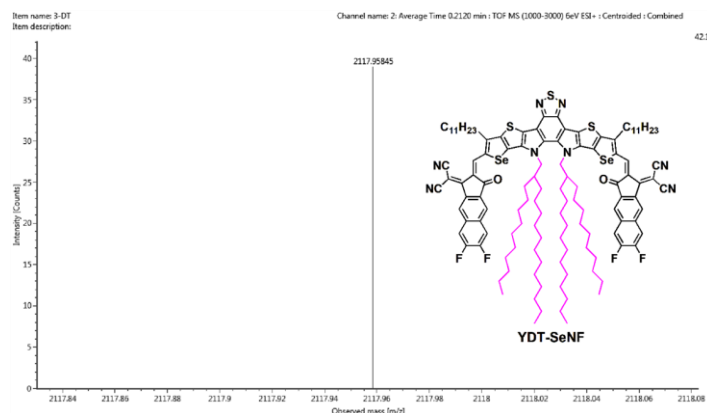


Fig. S12 MS image of YDT-SeNF

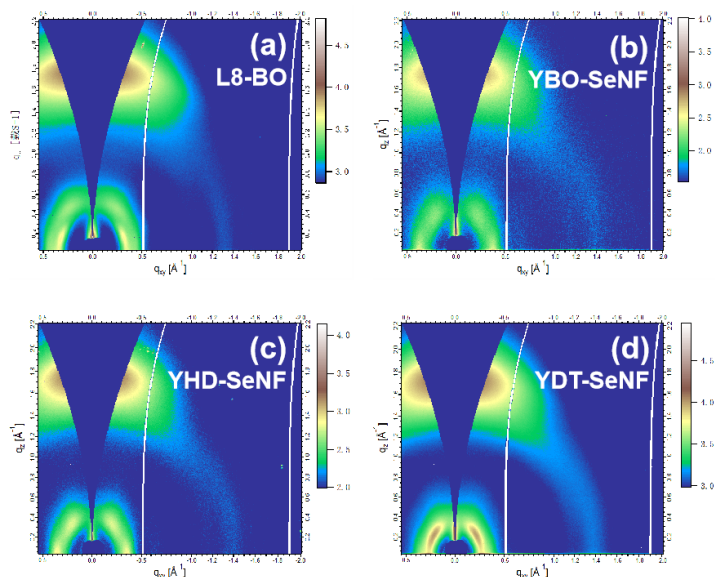


Fig. S13 2D-GIWAXS images of blade-coating neat films: (a) L8-BO, (b) YBO-SeNF, (c) YHD-SeNF, (d) YDT-SeNF, respectively

Table S1 GIWAXS test performance parameters of L8-BO and YR-SeNF neat films

	in plane					
	location (\AA^{-1})	d-spacing (\AA)	CCL (\AA)	location (\AA^{-1})	d-spacing (\AA)	CCL (\AA)
L8-BO	0.346	18.184	76.960	0.431	14.590	53.601
YBO-SeNF	0.376	16.696	53.990			
YHD-SeNF	0.352	17.853	53.464			
YDT-SeNF	0.267	23.565	75.185	0.342	18.355	59.385
	out of plane					
	location (\AA^{-1})	d-spacing (\AA)	CCL (\AA)	location (\AA^{-1})	d-spacing (\AA)	CCL (\AA)
L8-BO	1.734	3.624	16.472			
YBO-SeNF	1.717	3.659	16.572			
YHD-SeNF	1.701	3.694	16.269			
YDT-SeNF	1.686	3.726	15.010			

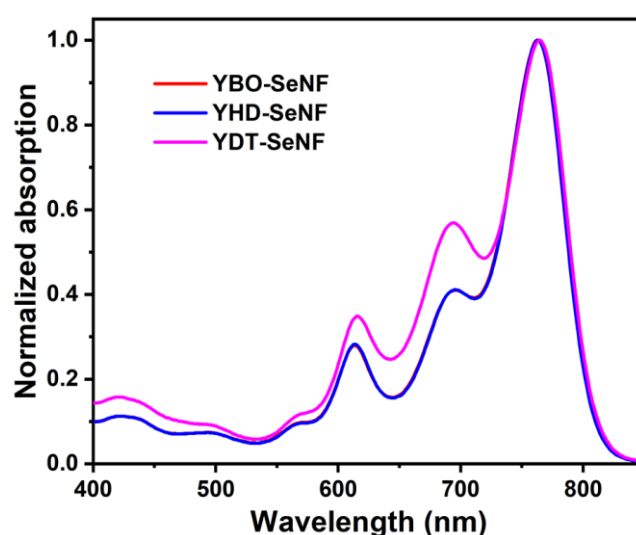


Fig. S14 Normalized absorption spectra of YR-SeNF series in dilute *o*-xylene solutions

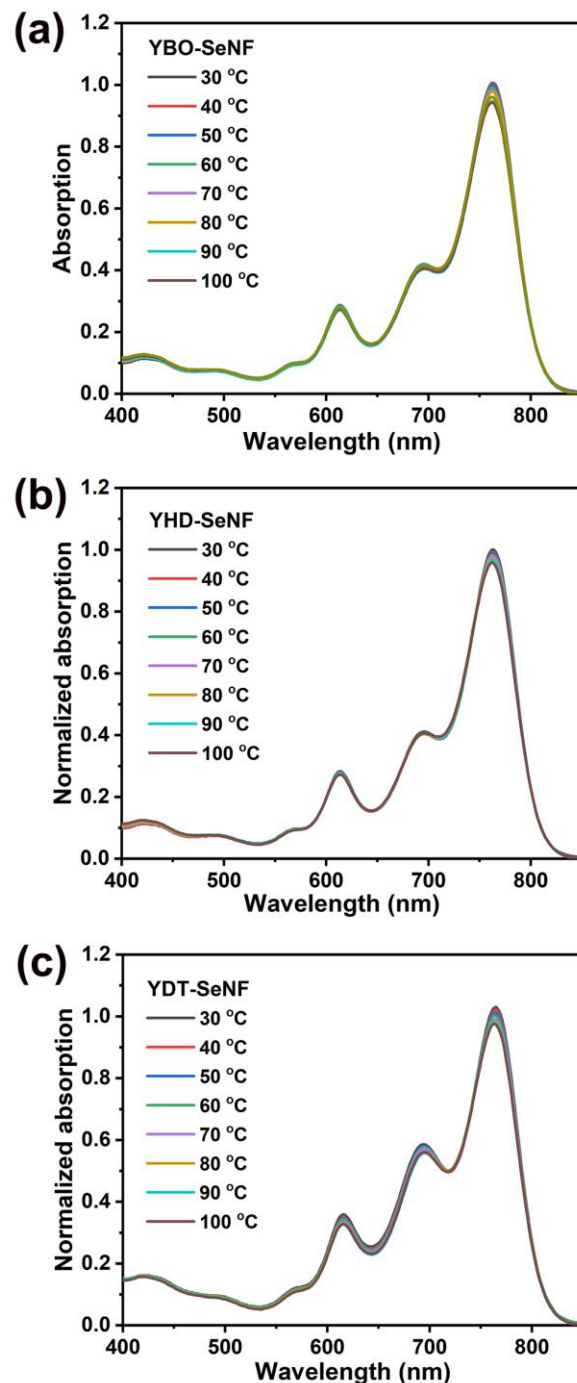


Fig. S15. Absorption spectra of YR-SeNF series in dilute *o*-xylene solutions with different temperatures: (a) YBO-SeNF, (b) YHD-SeNF, and (c) YDT-SeNF, respectively

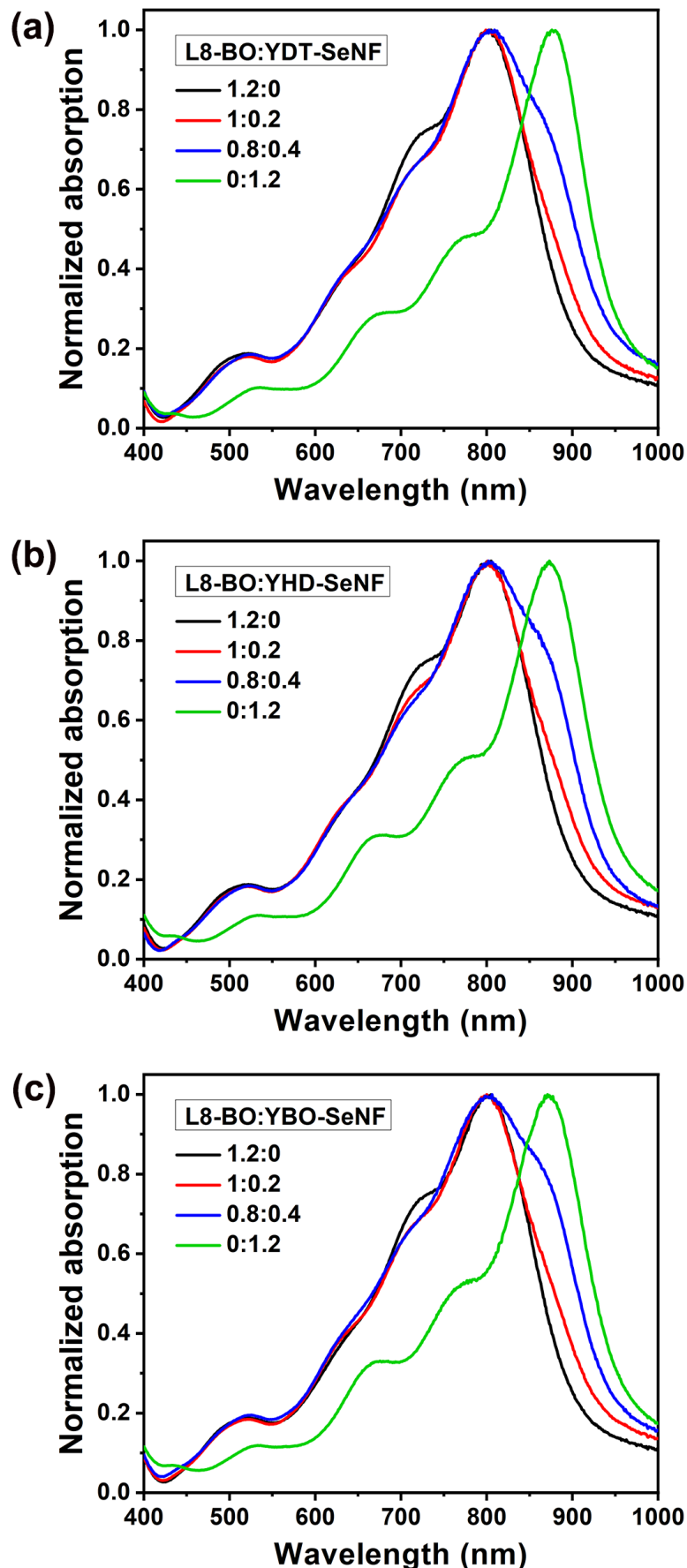


Fig. S16 Normalized absorption spectra of binary acceptor blends with different ratios: (a) L8-BO:YBO-SeNF, (b) L8-BO:YHD-SeNF, and (c) L8-BO:YDT-SeNF

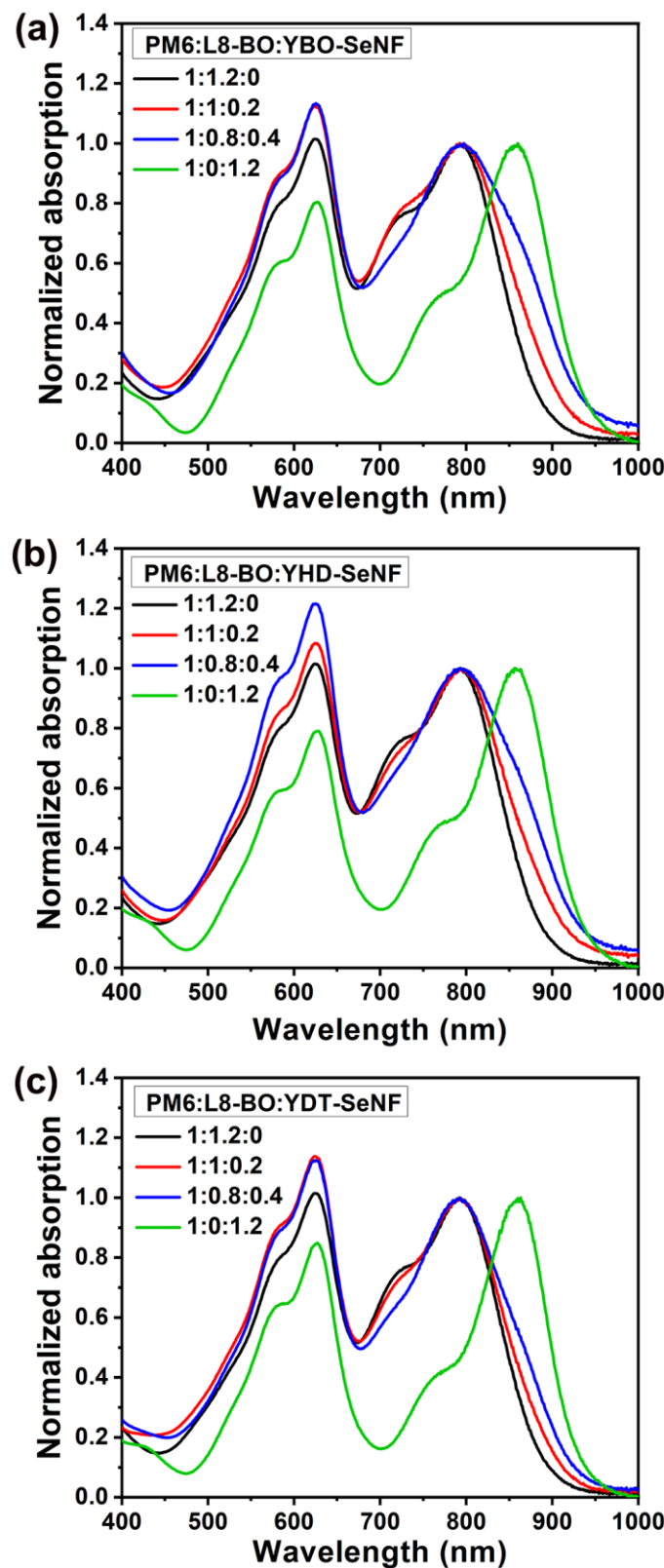


Fig. S17. Normalized absorption spectra of ternary active layers with different component ratios: (a) PM6:L8-BO:YBO-SeNF, (b) PM6:L8-BO:YHD-SeNF, and (c) PM6:L8-BO:YDT-SeNF

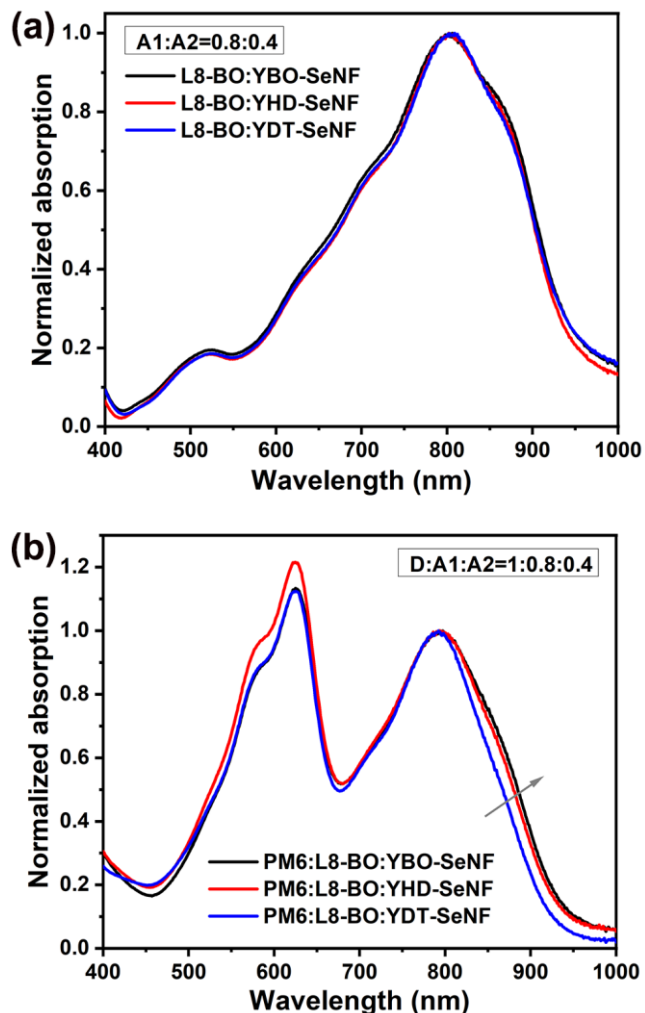


Fig. S18 Normalized absorption spectra of blend films: (a) binary L8-BO:YR-SeNF with a ratio of 0.8:0.4 and (b) ternary PM6:L8-BO:YR-SeNF with a ratio of 1:0.8:0.4

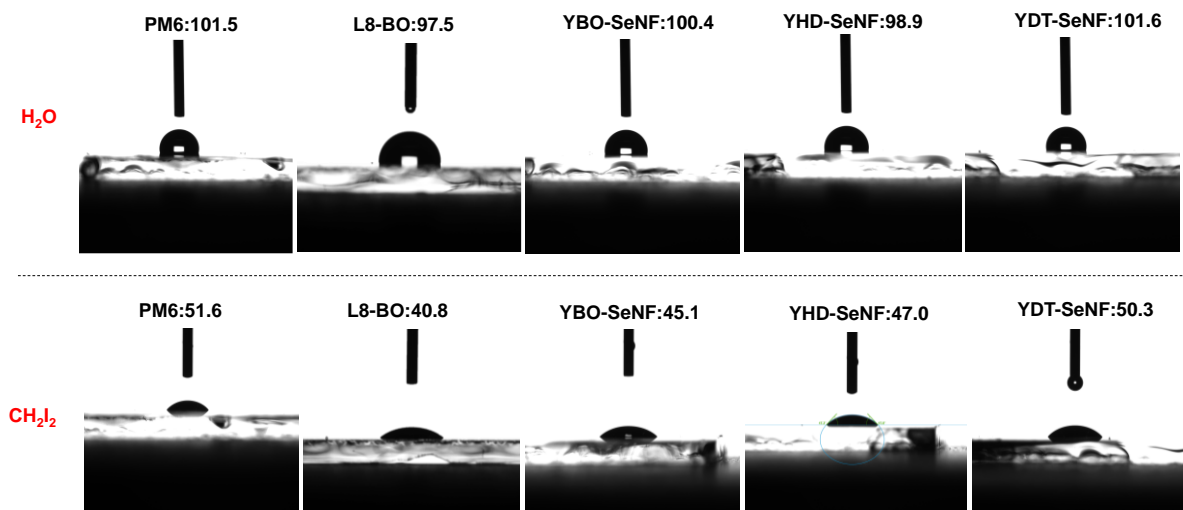


Fig. S19 Contact angle images of active layer materials in neat films on water (H₂O) and diiodomethane (CH₂I₂)

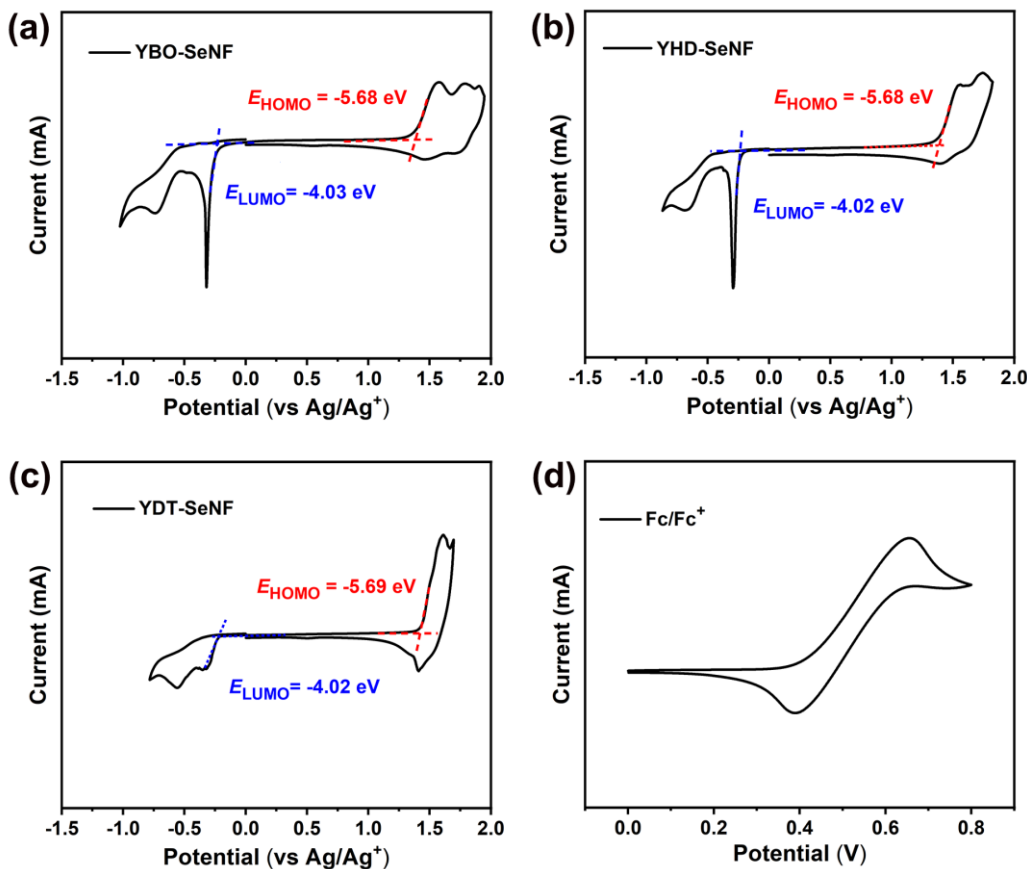


Fig. S20 Cyclic voltammograms of YR-SeNF neat films on a glassy carbon electrode measured in a 0.1 mol/L Bu₄NPF₆ acetonitrile solution at a scan rate of 50 mV/s

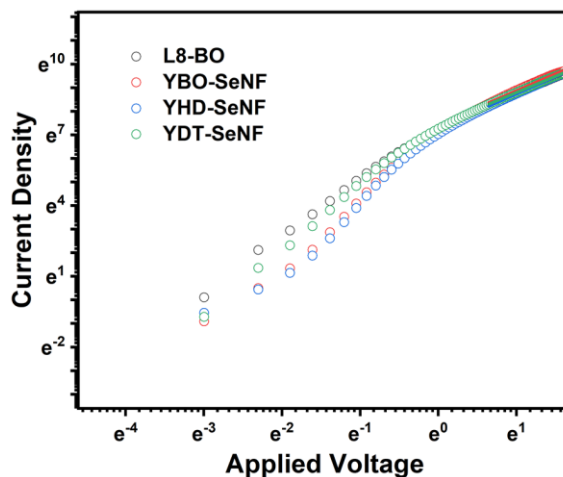


Fig. S21 Current density-applied voltage characteristics for the electron-only devices based on L8-BO and YR-SeNF neat films

Table S2 The charge mobilities of the electron-only devices according to the SCLC method

	μ_e (cm ² V ⁻¹ s ⁻¹)
L8-BO	1.82×10^{-3}
YBO-SeNF	1.94×10^{-3}
YHD-SeNF	1.65×10^{-3}
YDT-SeNF	1.90×10^{-3}

Table S3 Photovoltaic parameters of the OSCs based on active layers processed from halogen-free solvents

Active layers	Solvent	V _{OC} [V]	J _{SC} [mA cm ⁻²]	FF	PCE [%]	Refs.
PM6:L8-BO:YBO-SeNF (1:1:0.2)	<i>o</i> -xylene	0.869	27.3	0.776	18.4	This Work
PM6:L8-BO:YBO-SeNF (1:0.8:0.4)	<i>o</i> -xylene	0.861	27.5	0.772	18.2	This Work
PM6:L8-BO:YHD-SeNF (1:1:0.2)	<i>o</i> -xylene	0.874	27.3	0.789	18.8	This Work
PM6:L8-BO:YHD-SeNF (1:0.8:0.4)	<i>o</i> -xylene	0.866	28.0	0.775	18.8	This Work
PM6:L8-BO:YDT-SeNF (1:1:0.2)	<i>o</i> -xylene	0.871	26.9	0.788	18.5	This Work
PM6:L8-BO:YDT-SeNF (1:0.8:0.4)	<i>o</i> -xylene	0.864	27.8	0.775	18.6	This Work
PffBT4T-2DT:EH-IDTBR	Mesitylene	1.02	17.2	63.0	11.1	S8
PBQ-4F:ITIC	THF	0.95	17.87	66.8	11.34	S9
FTAZ:IT-M	Toluene	0.95	16.8	66.1	10.6	S10
PBDTS-TDZ:ITIC	<i>o</i> -xylene	1.1	17.78	65.4	12.8	S11
PBTA-TF:IT-M	<i>o</i> -xylene	0.97	17.76	71.0	12.2	S12
PBDB-BzT:IT-M	THF	0.96	17.63	0.69	11.68	S13
PM7:IT-4F	Toluene	0.88	20.9	71.1	13.1	S14
DRTT-T:F-2Cl	THF	1.0	16.82	62.6	10.45	S15
P19:ITIC	Toluene	0.938	15.68	68.03	10.01	S16
PTB-EDOTS:ITIC-Th	Me-THF	0.88	16.25	71.2	10.18	S17
DOTFP-PhI :IT-4F	Toluene	0.856	17.75	70.1	10.65	S18
P1:ITIC-Th	Toluene	1.01	17.89	63.05	11.39	S19
PM6:IT-4F	<i>o</i> -xylene	0.84	20.5	75.0	12.5	S20
P(Cl-Cl)(BDD=0.2):IT-4F	<i>o</i> -xylene	0.891	23.4	67.0	13.97	S21
PTB7-Th:ACS8	Toluene	0.75	25.3	69.3	13.2	S22
T1:IT-4F	THF	0.887	21.1	76.0	14.2	S23
T1:BTP-4F-12	THF	0.853	25.2	75.0	16.1	S24
PM6-Ir1.5:Y6-C2	Toluene	0.842	26.23	74.80	16.52	S25
PM6:DTY6	<i>o</i> -xylene	0.856	24.94	75.5	16.1	S26
PTQ10:HO-IDIC-2F	THF	0.91	18.52	70.77	12.2	S27
PMT50:BTP-4F-12	1,2,4-TMB	0.842	26.81	67.7	15.3	S28
PM6:BTP-BO-4Cl	Toluene	0.854	26.1	77.7	17.33	S29
PTzBI- <i>d</i> F:CH1007	<i>o</i> -xylene	0.82	27.3	73	17.3	S30
PM6:YSe-C6	<i>o</i> -xylene	0.85	25.94	73.0	16.11	S31

PM6:BTIC-2Cl- γ CF ₃	<i>o</i> -xylene	0.84	25.09	76.99	16.31	S32
PTQ10:m-DTC-2Cl/PTB7-Th: BTPV-4F-eC9	<i>o</i> -xylene/ THF	1.621	14.65	70.2	16.67	S33
PM6:PM7:Y6:20% BTO	Paraxylene	0.86	27.19	76.05	17.78	S34
PM6/BO-4F	<i>o</i> -xylene/ THF	0.82	26.2	74.3	16.0	S35
JD40-BDD20:PJTWT	<i>o</i> -xylene	0.91	23.88	75.54	16.35	S36
PBQ6:PYF-T- <i>o</i> /DTT	Toluene	0.886	25.12	76.64	17.06	S37
PM1:L8-BO:BTP-F3Cl	THF	0.876	27.4	78.4	18.8	S38
PM6:10%5BDTBDD:BT P-BO4Cl	<i>o</i> -xylene	0.843	26.83	77.43	17.54	S39
PL1:BTP-eC9-4F	<i>o</i> -xylene	0.876	27.11	76.41	18.14	S40
PM6:PYTCl-A	Toluene	0.939	21.71	72.12	14.7	S41
PBNT-TzTz:Y6-BO	Anisole	0.88	25.42	70.0	15.65	S42
PM6: BTP-eC9-HD	Toluene	0.83	26.6	78.8	17.5	S43

Table S4 Photovoltaic parameters of the OSCs based on active layers processed from spin-coating-free technologies

Active layers	Solvent	V _{oc} [V]	J _{SC} [mA cm ⁻²]	FF	PCE [%]	Refs.
PM6:L8-BO:YBO-SeNF (1:1:0.2)	blade-coating	0.869	27.3	0.776	18.4	This Work
PM6:L8-BO:YBO-SeNF (1:0.8:0.4)	blade-coating	0.861	27.5	0.772	18.2	This Work
PM6:L8-BO:YHD-SeNF (1:1:0.2)	blade-coating	0.874	27.3	0.789	18.8	This Work
PM6:L8-BO:YHD-SeNF (1:0.8:0.4)	blade-coating	0.866	28.0	0.775	18.8	This Work
PM6:L8-BO:YDT-SeNF (1:1:0.2)	blade-coating	0.871	26.9	0.788	18.5	This Work
PM6:L8-BO:YDT-SeNF (1:0.8:0.4)	blade-coating	0.864	27.8	0.775	18.6	This Work
PCDTBT:PC71BM (20 cm ²)	slot-die	0.88	10.66	55.2	5.18	S44
PffBT4T-2OD:PC71BM	blade-coating	0.77	18.4	70	9.9	S45
PTB7-Th:PC70BM	slot-die	2.36	4.98	62	8.1	S46
PBTA-TF:ITCC	blade-coating	1.0	15.54	67	10.4	S12
PBTA-TF:IT-M	blade-coating	0.97	17.76	71	12.2	S12
PBTA-TF:IT-4F	blade-coating	0.73	20.24	72	10.6	S12
PBDB-T:IT-M	blade-coating	0.73	24.61	65.51	12.02	S47
P3HT:IDTBR (60 cm ²)	slot-die	0.71	1.08	64.9	5.0	S48
PBDB-T-2F:IT-4F	blade-coating	0.86	21.3	76	13.9	S49
PBDB-T:ITIC	blade-coating	0.9	17.4	69	10.9	S49
PBDB-T:IT-M	blade-coating	0.94	16.9	71	11.3	S49

PBDB-T:IDIC	blade-coating	0.98	15.5	60	9.1	S49
PM6:IT-4F	blade-coating	0.82	18.9	64.0	9.9	S50
PM6:IT-4F:N2200	blade-coating	0.86	20.8	73.0	12.8	S50
PM6:Y6	blade-coating	0.81	24.4	66.0	12.6	S50
PM6:Y6:N2200	blade-coating	0.83	26.3	74.0	15.6	S50
PTB7-Th:PC ₇₁ BM	blade-coating	0.79	16.39	69.0	9.33	S51
PBDB-TF:IT-4F	blade-coating	0.86	20.8	72.0	12.88	S51
PM6:IT-4F	blade-coating	0.88	20.76	72.9	13.64	S52
PBDB-T:IT-M	blade-coating	0.93	16.8	76.0	11.8	S53
PNTz4T-5MTC:PC71BM (54.45 cm ²)	slot-die	7.97	1.34	61.0	6.61	S54
PBDTTT-EFT:PC71BM	blade-coating	0.82	19.44	63.0	9.75	S55
PBDTTT-EFT:PC71BM	blade-coating	0.85	17.39	67.0	9.39	S55
PBDTTT-EFT:PC71BM	blade-coating	0.82	17.89	74.0	11.09	S55
J71:ITC6-IC	blade-coating	0.96	17.61	67.54	11.42	S56
PTQ10:IDIC	blade-coating	0.952	17.14	69.13	11.28	S56
PBDB-T-SF:IT-4F	slot-die	0.87	20.13	70.11	12.3	S57
J71:ITC6-IC	blade-coating	0.968	16.85	70.1	11.47	S58
PCE10:Y8	blade-coating	0.703	20.53	60.65	8.75	S59
PCE10:Y8:ICBA	blade-coating	0.722	20.97	62.29	9.52	S59
PTB7-Th:F10IC2	blade-coating	0.766	23.8	68.5	12.5	S60
PBDB-TF:BTP-4Cl-8	blade-coating	0.838	21.7	63.5	11.5	S61
PBDB-TF:BTP-4Cl-12	blade-coating	0.833	26.0	71.6	15.5	S61
PBDB-TF:BTP-4Cl-16	blade-coating	0.807	19.4	68.9	10.8	S61
PT2:Y6	blade-coating	0.83	26.3	68.9	15.0	S62
PM6:Y6	blade-coating	0.834	25.9	75.68	16.35	S63
PM6:Y6-2Cl	blade-coating	0.849	25.88	72.3	15.89	S63
PTQ10:Y6	blade-coating	0.849	24.49	72.63	15.1	S63
PM6:Y6-C2	blade-coating	0.834	25.82	73.99	15.93	S63
PBDB-T:FOIC:IT-M	blade-coating	0.751	24.66	63.57	11.86	S64
PM6:Y6	blade-coating	0.834	24.9	74.6	15.51	S65
PM6:Y6	blade-coating	0.833	26.25	68.86	15.5	S66
PM6:BTP-eC9	blade-coating	0.839	25.87	77.0	16.71	S67

D18:BTR-Cl:Y6	slot-die	0.85	27.9	68.5	16.3	S68
PTQ10:Y6	blade-coating	0.842	25.6	67.1	14.5	S69
PM6:L8-BO (LBL)	slot-die	0.867	25.37	77.23	16.95	S70
PM6:T8 (BHJ)	slot-die	0.860	25.89	72.09	16.05	S71
PM6:T8 (LBL)	slot-die	0.866	26.21	74.29	16.86	S71
PM6:T8 (BHJ)	blade-coating	0.866	26.2	76.93	17.45	S71
PM6/T8 (LBL)	blade-coating	0.864	26.98	77.13	17.98	S71

Table S5 Photovoltaic data of the 20 independent OSCs based on PM6:L8-BO

	V_{OC} [V]	J_{SC} [mA cm $^{-2}$]	FF	PCE [%]		V_{OC} [V]	J_{SC} [mA cm $^{-2}$]	FF	PCE [%]
No.1	0.880	25.3	0.779	17.3	No.11	0.874	25.6	0.772	17.3
No.2	0.881	25.0	0.778	17.1	No.12	0.883	24.8	0.775	17.0
No.3	0.875	25.2	0.771	17.0	No.13	0.880	25.2	0.778	17.3
No.4	0.872	25.6	0.766	17.1	No.14	0.877	25.4	0.775	17.3
No.5	0.868	25.7	0.763	17.0	No.15	0.876	25.5	0.771	17.2
No.6	0.878	24.8	0.781	17.0	No.16	0.874	25.7	0.769	17.3
No.7	0.877	24.6	0.775	16.7	No.17	0.872	25.1	0.766	16.8
No.8	0.869	25.5	0.761	16.9	No.18	0.867	25.9	0.758	17.0
No.9	0.882	24.3	0.782	16.8	No.19	0.873	25.2	0.775	17.0
No.10	0.883	24.2	0.781	16.7	No.20	0.879	25	0.777	17.1

Table S6 Photovoltaic data of the 20 independent OSCs based on PM6:L8-BO:YBO-SeNF (1:1:0.2)

	V_{OC} [V]	J_{SC} [mA cm $^{-2}$]	FF	PCE [%]		V_{OC} [V]	J_{SC} [mA cm $^{-2}$]	FF	PCE [%]
No.1	0.869	27.3	0.776	18.4	No.11	0.868	27.2	0.775	18.3
No.2	0.865	27.1	0.772	18.1	No.12	0.863	26.7	0.765	17.6
No.3	0.859	27.5	0.768	18.1	No.13	0.862	26.8	0.758	17.5
No.4	0.855	26.8	0.778	17.8	No.14	0.868	27.5	0.765	18.3
No.5	0.862	27.2	0.771	18.1	No.15	0.868	27.2	0.777	18.3
No.6	0.863	27.1	0.766	17.9	No.16	0.869	26.8	0.78	18.2
No.7	0.861	26.7	0.781	18.0	No.17	0.872	26.2	0.782	17.9

No.8	0.872	26.1	0.782	17.8	No.18	0.867	27.1	0.778	18.3
No.9	0.861	27	0.775	18.0	No.19	0.865	27	0.775	18.1
No.10	0.87	26.8	0.772	18.0	No.20	0.866	26.5	0.778	17.9

Table S7 Photovoltaic data of the 20 independent OSCs based on PM6:L8-BO:YBO-SeNF (1:0.8:0.4)

	V_{OC} [V]	J_{SC} [mA cm ⁻²]	FF	PCE [%]		V_{OC} [V]	J_{SC} [mA cm ⁻²]	FF	PCE [%]
No.1	0.861	27.5	0.772	18.2	No.11	0.854	27.6	0.759	17.9
No.2	0.862	27	0.775	18.0	No.12	0.860	27.4	0.774	18.2
No.3	0.860	27.6	0.765	18.2	No.13	0.861	27.3	0.77	18.1
No.4	0.855	27.3	0.758	17.7	No.14	0.862	27.1	0.769	18.0
No.5	0.856	27.2	0.761	17.7	No.15	0.859	27.7	0.766	18.2
No.6	0.851	27.8	0.755	17.9	No.16	0.858	27.5	0.772	18.2
No.7	0.852	27.6	0.766	18.0	No.17	0.860	27.1	0.771	18.0
No.8	0.856	27.2	0.768	17.9	No.18	0.853	27.6	0.763	18.0
No.9	0.852	26.8	0.771	17.6	No.19	0.852	27.1	0.77	17.8
No.10	0.862	26.3	0.773	17.5	No.20	0.857	26.9	0.768	17.7

Table S8 Photovoltaic data of the 20 independent OSCs based on PM6:YBO-SeNF

	V_{OC} [V]	J_{SC} [mA cm ⁻²]	FF	PCE [%]		V_{OC} [V]	J_{SC} [mA cm ⁻²]	FF	PCE [%]
No.1	0.824	27.1	0.745	16.6	No.11	0.820	26.5	0.740	16.1
No.2	0.818	27.3	0.728	16.3	No.12	0.817	27	0.732	16.1
No.3	0.811	27.5	0.719	16.0	No.13	0.827	26.6	0.742	16.3
No.4	0.825	26.5	0.742	16.2	No.14	0.822	26.9	0.735	16.3
No.5	0.828	26.3	0.746	16.2	No.15	0.819	27.5	0.711	16.0
No.6	0.829	25.9	0.741	15.9	No.16	0.813	27.6	0.714	16.0
No.7	0.812	27.2	0.716	15.8	No.17	0.825	27	0.742	16.5
No.8	0.816	26.5	0.725	15.7	No.18	0.829	26	0.751	16.2
No.9	0.823	26.7	0.737	16.2	No.19	0.824	26.7	0.747	16.4
No.10	0.822	26.9	0.746	16.5	No.20	0.821	26.5	0.732	15.9

Table S9 Photovoltaic data of the 20 independent OSCs based on PM6:L8-BO:YHD-SeNF (1:1:0.2)

	V_{OC} [V]	J_{SC} [mA cm $^{-2}$]	FF	PCE [%]		V_{OC} [V]	J_{SC} [mA cm $^{-2}$]	FF	PCE [%]
No.1	0.874	27.3	0.789	18.8	No.11	0.871	26.8	0.785	18.3
No.2	0.871	27.1	0.785	18.5	No.12	0.88	26.1	0.793	18.2
No.3	0.867	27.5	0.776	18.5	No.13	0.873	27.2	0.786	18.7
No.4	0.878	26.2	0.792	18.2	No.14	0.874	27.2	0.788	18.7
No.5	0.870	27.6	0.781	18.8	No.15	0.875	27.0	0.782	18.5
No.6	0.868	27.5	0.78	18.6	No.16	0.879	26.4	0.788	18.3
No.7	0.859	27.2	0.776	18.1	No.17	0.872	27.1	0.782	18.5
No.8	0.862	27.6	0.772	18.4	No.18	0.871	27.0	0.777	18.3
No.9	0.871	26.6	0.776	18.0	No.19	0.874	27.3	0.783	18.7
No.10	0.873	27.0	0.772	18.2	No.20	0.875	27.2	0.781	18.6

Table S10 Photovoltaic data of the 20 independent OSCs based on PM6:L8-BO:YHD-SeNF (1:0.8:0.4)

	V_{OC} [V]	J_{SC} [mA cm $^{-2}$]	FF	PCE [%]		V_{OC} [V]	J_{SC} [mA cm $^{-2}$]	FF	PCE [%]
No.1	0.866	28.0	0.775	18.8	No.11	0.852	28.1	0.759	18.2
No.2	0.862	28.2	0.766	18.6	No.12	0.851	27.9	0.763	18.1
No.3	0.86	28.0	0.763	18.4	No.13	0.857	27.5	0.77	18.1
No.4	0.852	28.5	0.758	18.4	No.14	0.865	27.1	0.772	18.1
No.5	0.855	28.1	0.763	18.3	No.15	0.866	27.2	0.778	18.3
No.6	0.868	27.6	0.776	18.6	No.16	0.861	28.3	0.761	18.5
No.7	0.867	27.2	0.779	18.4	No.17	0.865	28.1	0.773	18.8
No.8	0.861	27.9	0.775	18.6	No.18	0.853	27.5	0.758	17.8
No.9	0.857	28.3	0.773	18.7	No.19	0.849	28.8	0.745	18.2
No.10	0.855	27.7	0.769	18.2	No.20	0.869	26.9	0.776	18.1

Table S11 Photovoltaic data of the 20 independent OSCs based on PM6:YHD-SeNF

	V_{OC} [V]	J_{SC} [mA cm $^{-2}$]	FF	PCE [%]		V_{OC} [V]	J_{SC} [mA cm $^{-2}$]	FF	PCE [%]
No.1	0.848	26.4	0.753	16.8	No.11	0.844	25.9	0.760	16.6
No.2	0.853	25.5	0.755	16.4	No.12	0.84	25.7	0.739	16.0
No.3	0.847	26.2	0.750	16.6	No.13	0.826	26.6	0.722	15.9

No.4	0.842	26.5	0.749	16.7	No.14	0.839	25.5	0.734	15.7
No.5	0.843	26.0	0.742	16.3	No.15	0.842	25.3	0.758	16.1
No.6	0.837	26.3	0.749	16.5	No.16	0.832	26.1	0.748	16.2
No.7	0.835	25.8	0.752	16.2	No.17	0.837	26.2	0.741	16.2
No.8	0.831	26.7	0.733	16.3	No.18	0.833	25.9	0.739	15.9
No.9	0.841	25.8	0.729	15.8	No.19	0.841	25.2	0.756	16.0
No.10	0.828	26.5	0.736	16.1	No.20	0.849	26.1	0.751	16.6

Table S12 Photovoltaic data of the 20 independent OSCs based on PM6:L8-BO:YDT-SeNF (1:1:0.2)

	V _{OC} [V]	J _{SC} [mA cm ⁻²]	FF	PCE [%]		V _{OC} [V]	J _{SC} [mA cm ⁻²]	FF	PCE [%]
No.1	0.871	26.9	0.788	18.5	No.11	0.856	27.4	0.770	18.1
No.2	0.865	26.5	0.785	18.0	No.12	0.869	26.2	0.784	17.8
No.3	0.866	27.0	0.781	18.3	No.13	0.862	27.1	0.787	18.4
No.4	0.860	27.2	0.773	18.1	No.14	0.875	25.9	0.795	18.0
No.5	0.872	26.3	0.791	18.1	No.15	0.869	27.2	0.780	18.4
No.6	0.857	27.1	0.772	17.9	No.16	0.861	27.0	0.778	18.1
No.7	0.858	26.8	0.783	18.0	No.17	0.865	26.2	0.783	17.7
No.8	0.864	27.0	0.769	17.9	No.18	0.870	26.5	0.784	18.1
No.9	0.873	26.3	0.774	17.8	No.19	0.862	26.9	0.779	18.1
No.10	0.870	26.5	0.791	18.2	No.20	0.855	27.2	0.782	18.2

Table S13 Photovoltaic data of the 20 independent OSCs based on PM6:L8-BO:YDT-SeNF (1:0.8:0.4)

	V _{OC} [V]	J _{SC} [mA cm ⁻²]	FF	PCE [%]		V _{OC} [V]	J _{SC} [mA cm ⁻²]	FF	PCE [%]
No.1	0.864	27.8	0.775	18.6	No.11	0.847	28.2	0.762	18.2
No.2	0.860	28.0	0.771	18.6	No.12	0.858	27.6	0.777	18.4
No.3	0.852	27.6	0.762	17.9	No.13	0.856	27.9	0.770	18.4
No.4	0.856	27.1	0.769	17.8	No.14	0.867	26.6	0.780	18.0
No.5	0.852	27.5	0.772	18.1	No.15	0.863	27.2	0.782	18.4
No.6	0.857	27.5	0.776	18.3	No.16	0.865	27.5	0.771	18.3
No.7	0.866	26.9	0.766	17.8	No.17	0.866	27.1	0.780	18.3
No.8	0.867	27.2	0.778	18.3	No.18	0.853	28.2	0.767	18.4

No.9	0.863	27.9	0.772	18.6	No.19	0.852	27.5	0.764	17.9
No.10	0.848	28.1	0.769	18.3	No.20	0.861	27.7	0.773	18.4

Table S14 Photovoltaic data of the 20 independent OSCs based on PM6:YDT-SeNF

	V _{OC} [V]	J _{SC} [mA cm ⁻²]	FF	PCE [%]		V _{OC} [V]	J _{SC} [mA cm ⁻²]	FF	PCE [%]
No.1	0.836	27.2	0.754	17.2	No.11	0.838	26.7	0.759	17.0
No.2	0.828	27.3	0.746	16.9	No.12	0.833	27.5	0.744	17.0
No.3	0.823	27.6	0.739	16.8	No.13	0.819	27.7	0.729	16.5
No.4	0.837	26.1	0.761	16.6	No.14	0.818	27.8	0.736	16.7
No.5	0.836	26.3	0.755	16.6	No.15	0.822	27.6	0.730	16.6
No.6	0.834	27.0	0.755	17.0	No.16	0.827	27.0	0.744	16.6
No.7	0.827	26.9	0.743	16.5	No.17	0.837	26.7	0.755	16.9
No.8	0.829	27.1	0.751	16.9	No.18	0.841	26.5	0.753	16.8
No.9	0.834	26.7	0.754	16.8	No.19	0.831	27.7	0.732	16.8
No.10	0.840	26.3	0.761	16.8	No.20	0.825	28.0	0.726	16.8

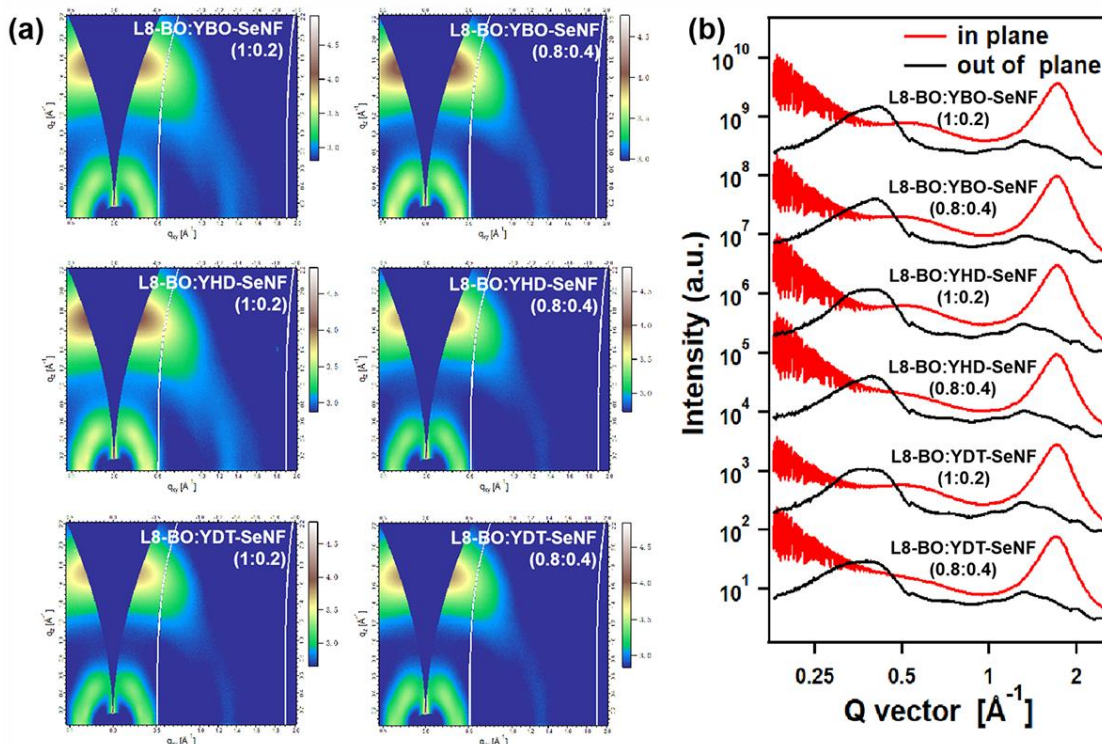


Fig. S22 (a) GIWAXS profiles of blade-coating L8-BO:YR-SeNF (1:0.2 and 0.8:0.4) binary blends and (b) the corresponding line-cuts

Table S15 GIWAXS test performance parameters of L8-BO:YR-SeNF binary blends

	in plane					
	location (Å ⁻¹)	d-spacing (Å)	CCL (Å)	location (Å ⁻¹)	d-spacing (Å)	CCL (Å)
L8-BO:YBO-SeNF (1:0.2)	0.341	18.438	49.181	0.425	14.783	54.160
L8-BO:YBO-SeNF (0.8:0.4)	0.343	18.308	40.467	0.419	15.007	56.273
L8-BO:YHD-SeNF (1:0.2)	0.341	18.399	50.798	0.425	14.785	45.766
L8-BO:YHD-SeNF (0.8:0.4)	0.336	18.715	44.962	0.412	15.247	55.083
L8-BO:YDT-SeNF (1:0.2)	0.352	17.858	46.083	0.432	14.532	67.185
L8-BO:YDT-SeNF (0.8:0.4)	0.319	19.671	45.655	0.409	15.345	51.516
out of plane						
	location (Å ⁻¹)	d-spacing (Å)	CCL (Å)	location (Å ⁻¹)	d-spacing (Å)	CCL (Å)
L8-BO:YBO-SeNF (1:0.2)	1.721	3.651	16.247			
L8-BO:YBO-SeNF (0.8:0.4)	1.712	3.671	16.487			
L8-BO:YHD-SeNF (1:0.2)	1.713	3.667	16.502			
L8-BO:YHD-SeNF (0.8:0.4)	1.710	3.675	16.288			
L8-BO:YDT-SeNF (1:0.2)	1.710	3.674	16.023			
L8-BO:YDT-SeNF (0.8:0.4)	1.700	3.697	16.009			

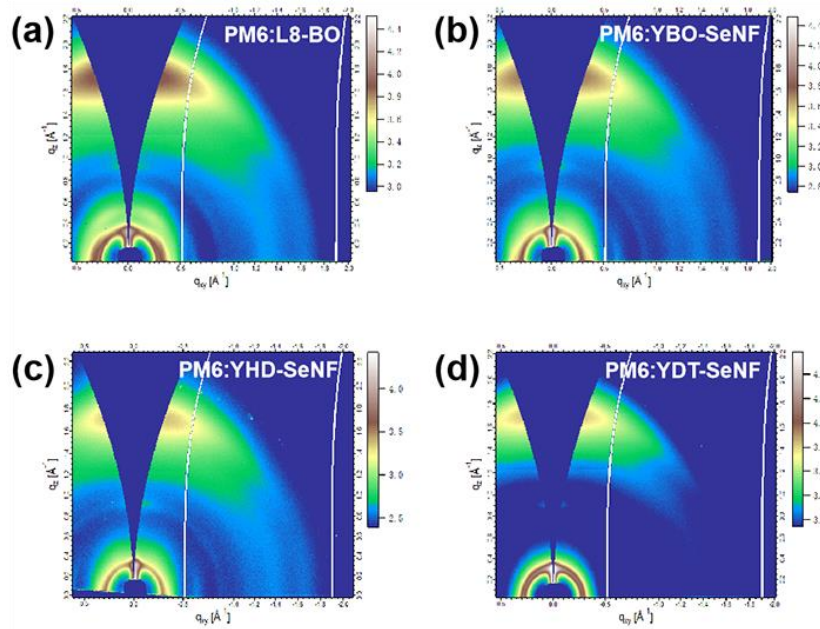


Fig. S23 GIWAXS profiles of blade-coating binary blends of (a) PM6:L8-BO, (b) PM6:YBO-SeNF, (c) PM6:YHD-SeNF, and (d) PM6:YDT-SeNF

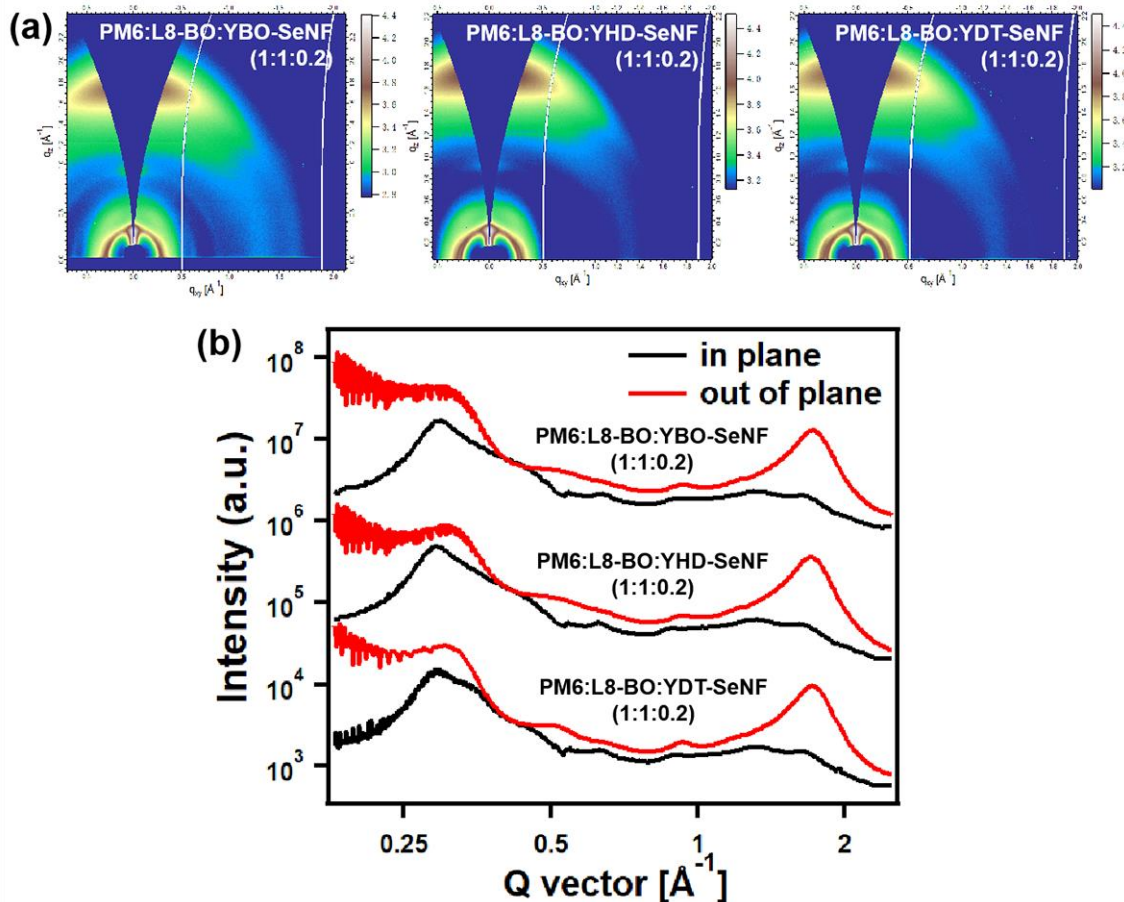


Fig. S24 (a) GIWAXS profiles of blade-coating PM6:L8-BO:YR-SeNF (1:1:0.2) blends and (b) the corresponding line-cuts

Table S16 GIWAXS test performance parameters of PM6:L8-BO:YR-SeNF blends with different component ratios

	in plane					
	location (Å ⁻¹)	d-spacing (Å)	CCL (Å)	location (Å ⁻¹)	d-spacing (Å)	CCL (Å)
PM6:L8-BO:YBO-SeNF (1:1:2:0)	0.293	21.426	94.764	0.348	18.081	111.04
	0.403	15.608	52.326			
PM6:L8-BO:YBO-SeNF (1:1:0.2)	0.297	21.151	91.900	0.354	17.766	129.91
	0.398	15.780	56.374			
PM6:L8-BO:YBO-SeNF (1:0.8:0.4)	0.296	21.259	93.676	0.352	17.834	136.26
	0.395	15.890	69.113			
PM6:L8-BO:YBO-SeNF (1:0:1.2)	0.293	21.470	101.12	0.361	17.405	56.603
PM6:L8-BO:YHD-SeNF (1:1:0.2)	0.291	21.618	114.10	0.347	18.109	124.41
	0.394	15.941	52.889			
PM6:L8-BO:YHD-SeNF (1:0.8:0.4)	0.294	21.379	96.664	0.348	18.058	127.55
	0.392	16.044	61.455			
PM6:L8-BO:YHD-SeNF (1:0:1.2)	0.293	21.479	94.414	0.354	17.750	66.232
PM6:L8-BO:YDT-SeNF (1:1:0.2)	0.292	21.514	98.263	0.345	18.217	113.12
	0.402	15.613	60.009			
PM6:L8-BO:YDT-SeNF (1:0.8:0.4)	0.294	21.348	81.951	0.358	17.561	120.02
	0.402	15.610	52.574			
PM6:L8-BO:YDT-SeNF (1:0:1.2)	0.285	22.045	87.276			
out of plane						
	location (Å ⁻¹)	d-spacing (Å)	CCL (Å)	location (Å ⁻¹)	d-spacing (Å)	CCL (Å)
PM6:L8-BO:YBO-SeNF (1:1:2:0)	1.709	3.677	17.231			
PM6:L8-BO:YBO-SeNF (1:1:0.2)	1.713	3.668	17.863			
PM6:L8-BO:YBO-SeNF (1:0.8:0.4)	1.709	3.676	17.995			
PM6:L8-BO:YBO-SeNF (1:0:1.2)	1.706	3.684	16.963			
PM6:L8-BO:YHD-SeNF	1.697	3.702	16.918			

(1:1:0.2)			
PM6:L8-BO:YHD-SeNF (1:0.8:0.4)	1.695	3.705	16.628
PM6:L8-BO:YHD-SeNF (1:0:1.2)	1.690	3.717	16.359
PM6:L8-BO:YDT-SeNF (1:1:0.2)	1.707	3.681	17.126
PM6:L8-BO:YDT-SeNF (1:0.8:0.4)	1.690	3.718	16.432
PM6:L8-BO:YDT-SeNF (1:0:1.2)	1.676	3.749	15.361

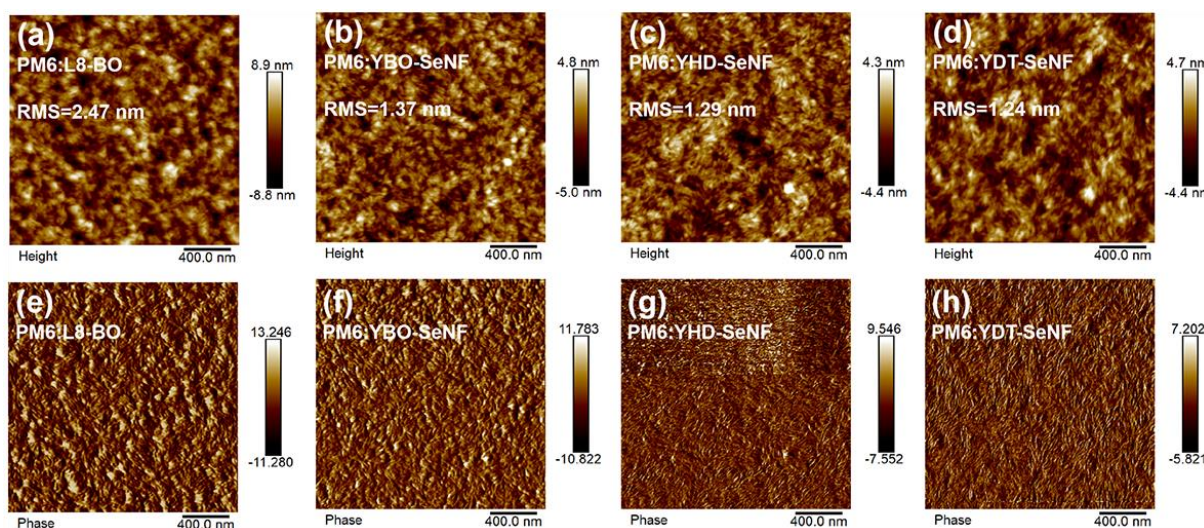


Fig. S25 AFM height images (a-d) and phase images (e-h) of PM6:L8-BO and PM6:YR-SeNF binary blends

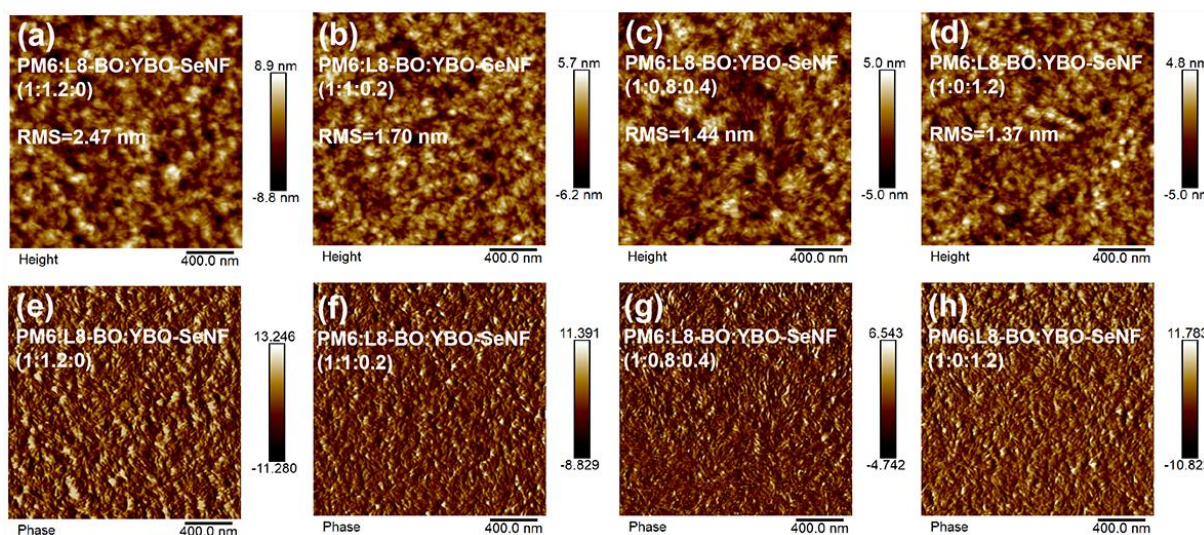


Fig. S26 AFM height images (a-d) and phase images (e-h) of PM6:L8-BO:YBO-SeNF blends with different component ratios

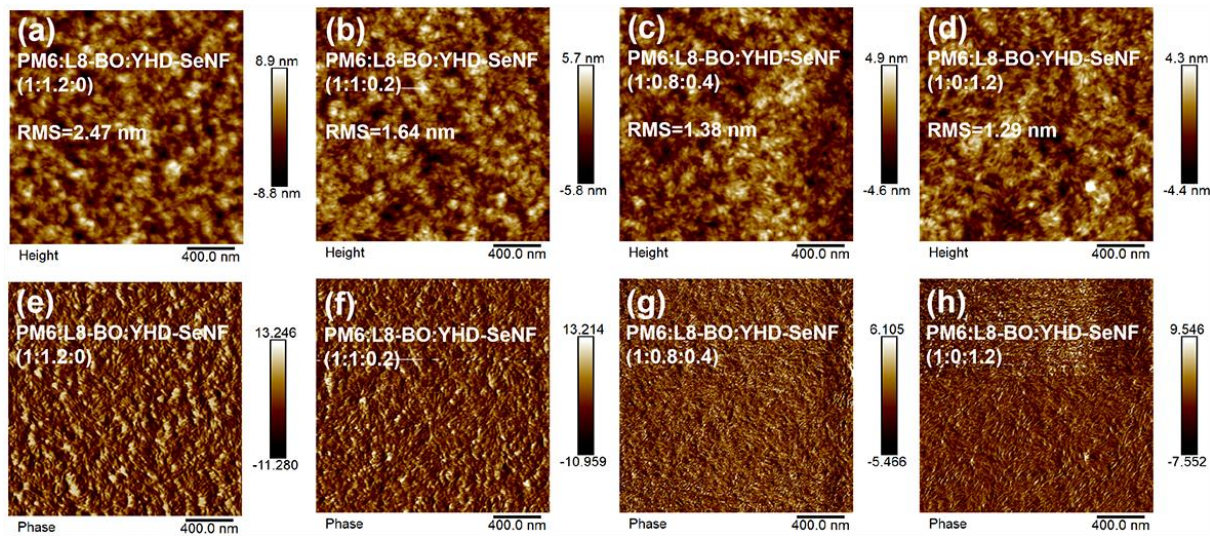


Fig. S27 AFM height images (**a-d**) and phase images (**e-h**) of PM6:L8-BO:YHD-SeNF blends with different component ratios

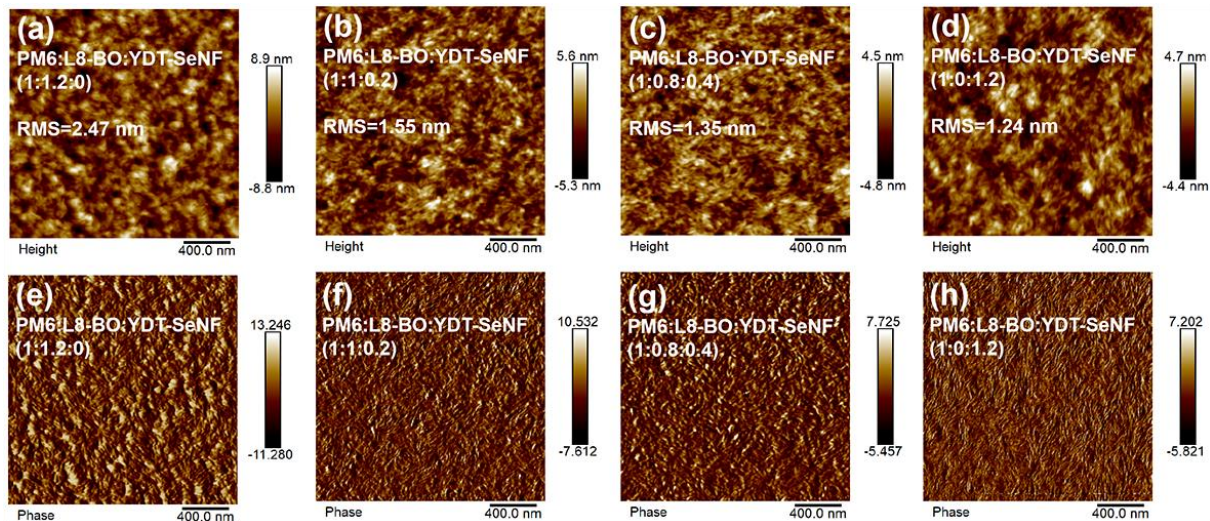


Fig. S28 AFM height images (**a-d**) and phase images (**e-h**) of PM6:L8-BO:YDT-SeNF blends with different component ratios

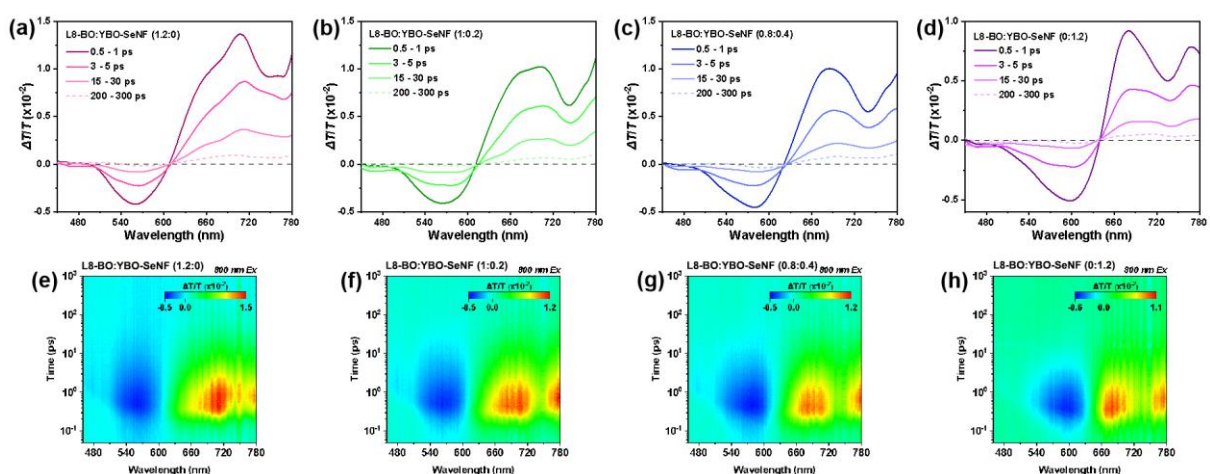


Fig. S29 (**a-d**) Spectral line-cuts in terms of $\Delta T/T$ at representative times and (**e-h**) fs-TAS profiles of L8-BO:YBO-SeNF films with different component ratios

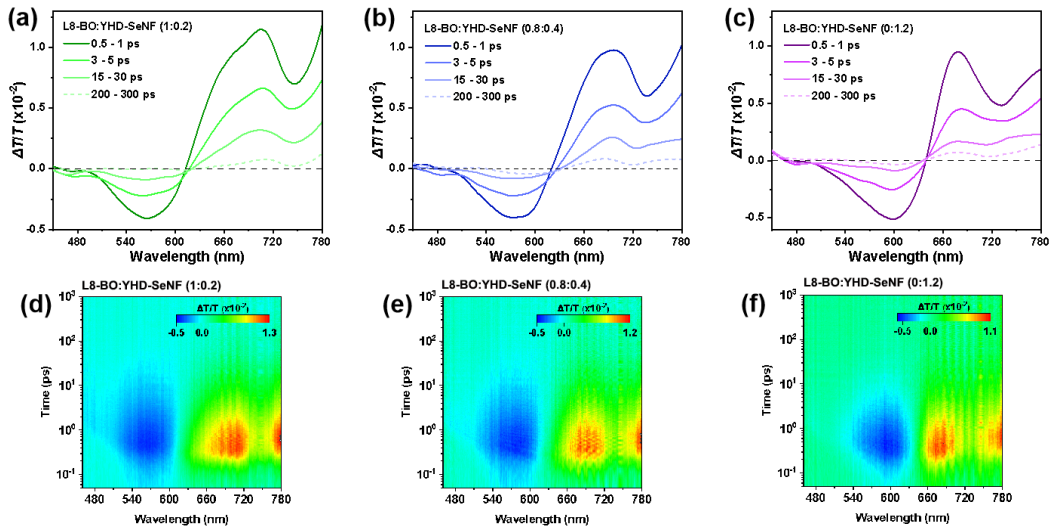


Fig. S30 (a-c) Spectral line-cuts in terms of $\Delta T/T$ at representative times and (d-f) fs-TAS profiles of L8-BO:YHD-SeNF films with different component ratios

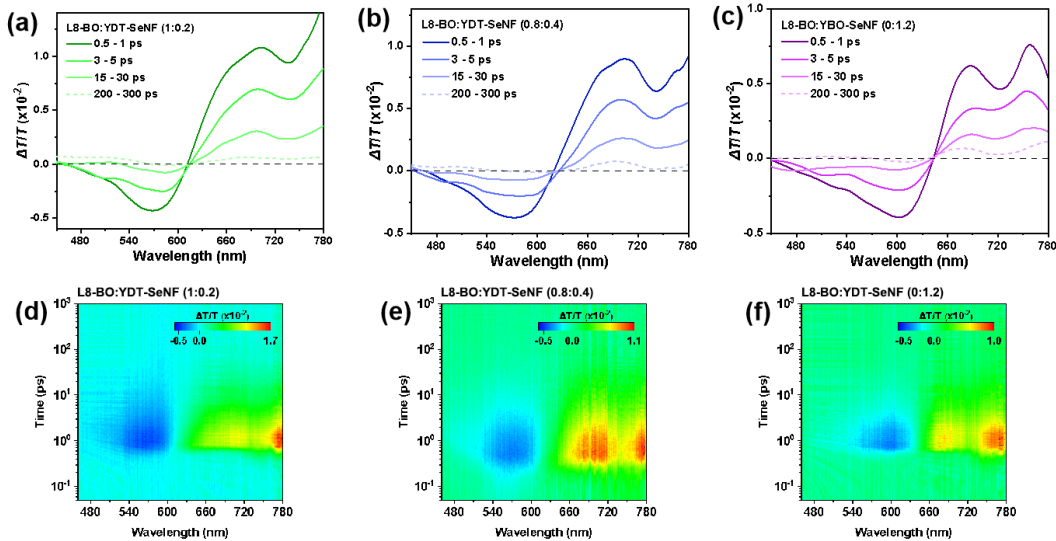


Fig. S31 (a-c) Spectral line-cuts in terms of $\Delta T/T$ at representative times and (d-f) fs-TAS profiles of L8-BO:YDT-SeNF films with different component ratios

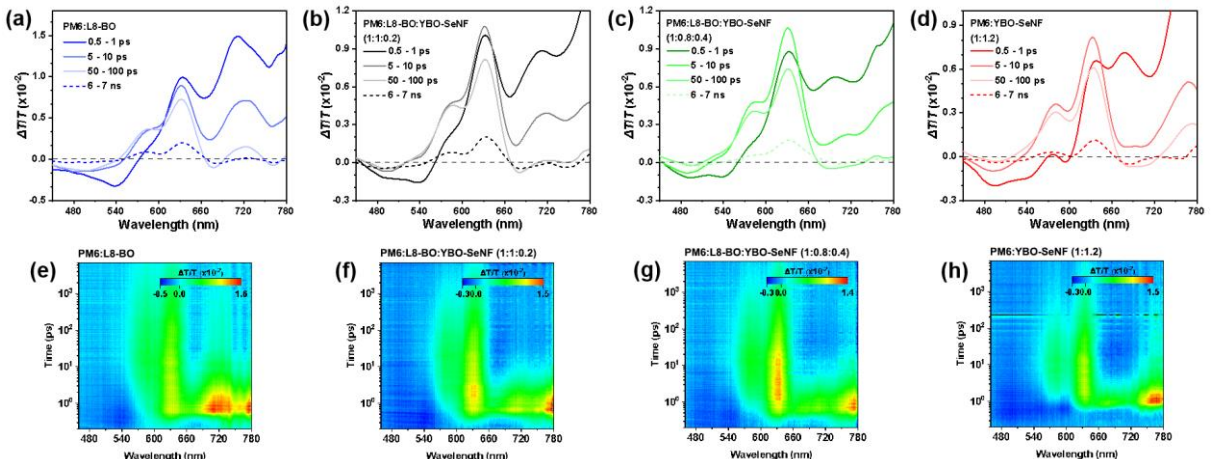


Fig. S32 (a-d) Spectral line-cuts in terms of $\Delta T/T$ at representative times and (e-h) fs-TAS profiles of PM6:L8-BO:YBO-SeNF blend films with different component ratios

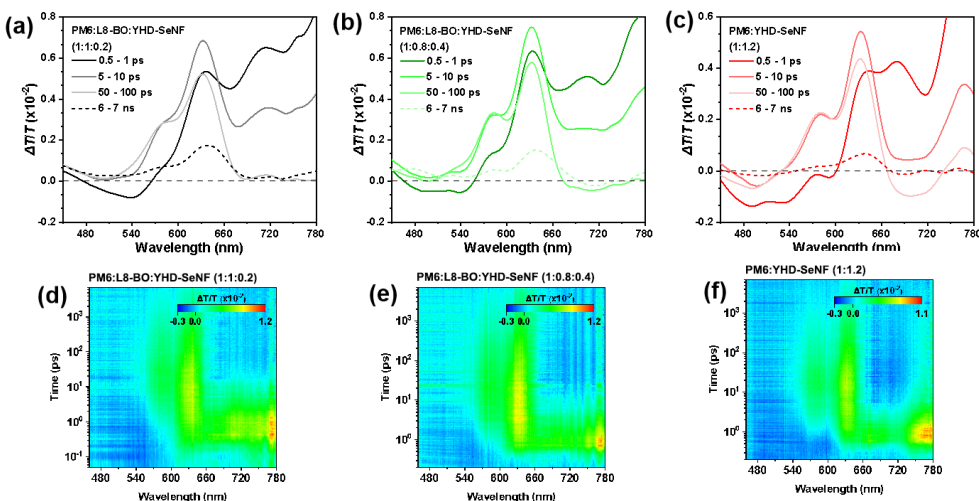


Fig. S33 (a-c) Spectral line-cuts in terms of $\Delta T/T$ at representative times and (d-f) fs-TAS profiles of PM6:L8-BO:YHD-SeNF blend films with different component ratios

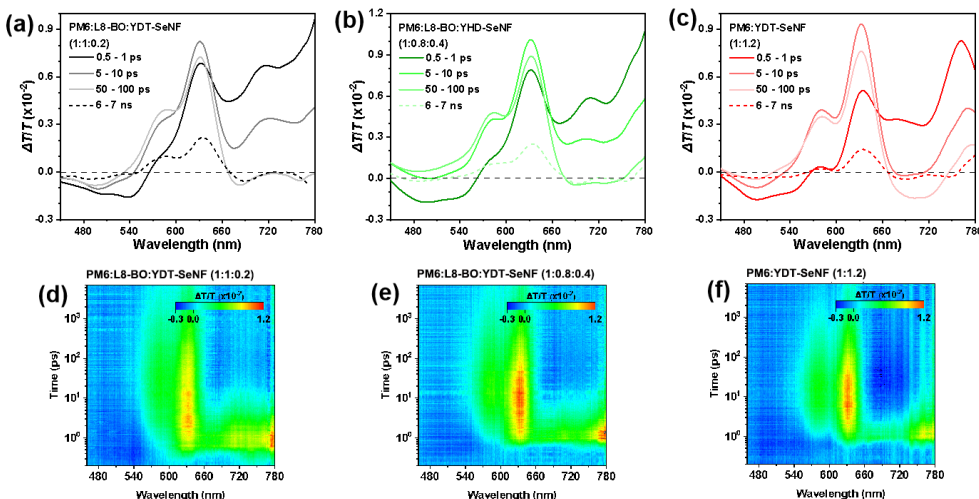


Fig. S34 (a-c) Spectral line-cuts in terms of $\Delta T/T$ at representative times and (d-f) fs-TAS profiles of PM6:L8-BO:YDT-SeNF blend films with different component ratios

Supplementary References

- [S1] Y. Cui, H. Yao, J. Zhang, K. Xian, T. Zhang et al., Single-Junction Organic Photovoltaic Cells with Approaching 18% Efficiency. *Adv. Mater.* 32, 1908205 (2020). <https://doi.org/10.1002/adma.201908205>
- [S2] F. Lin, K. Jiang, W. Kaminsky, Z. Zhu, A. K. Y. Jen, A Non-fullerene Acceptor with Enhanced Intermolecular π -Core Interaction for High-Performance Organic Solar Cells. *J. Am. Chem. Soc.* 142, 15246-15251 (2020). <https://doi.org/10.1021/jacs.0c07083>
- [S3] Q. Fan, R. Ma, W. Su, Q. Zhu, Z. Luo et al., A new perspective to develop regiorandom polymer acceptors with high active layer ductility, excellent device stability, and high efficiency approaching 17%. *Carbon Energy* 5, e267 (2023). <https://doi.org/10.1002/cey2.267>
- [S4] C. Li, J. Zhou, J. Song, J. Xu, H. Zhang et al., Non-fullerene acceptors with branched side chains and improved molecular packing to exceed 18% efficiency in organic solar cells. *Nat. Energy* 6, 605-613 (2021). <https://doi.org/10.1038/s41560-021-00820-x>

- [S5] M. Zhang, X. Guo, W. Ma, H. Ade, J. Hou, A Large-Bandgap Conjugated Polymer for Versatile Photovoltaic Applications with High Performance. *Adv. Mater.* 27, 4655-4660 (2015). <https://doi.org/10.1002/adma.201502110>
- [S6] Y. Shi, J. Pan, J. Yu, J. Zhang, F. Gao et al., Optimizing the Charge Carrier and Light Management of Nonfullerene Acceptors for Efficient Organic Solar Cells with Small Nonradiative Energy Losses. *Sol. RRL* 5, 2100008 (2021). <https://doi.org/10.1002/solr.202100008>
- [S7] J. Yin, K. Chaitanya, X.-H. Ju, Bromination and cyanation for improving electron transport performance of anthra-tetrathiophene. *J. Mater. Res.* 31, 337-347 (2016). <https://doi.org/10.1557/jmr.2016.8>
- [S8] A. Wadsworth, R. S. Ashraf, M. Abdelsamie, S. Pont, M. Little et al., Highly Efficient and Reproducible Nonfullerene Solar Cells from Hydrocarbon Solvents. *ACS Energy Lett.* 2, 1494-1500 (2017). <https://doi.org/10.1021/acsenergylett.7b00390>
- [S9] Z. Zheng, O. M. Awartani, B. Gautam, D. Liu, Y. Qin et al., Efficient Charge Transfer and Fine-Tuned Energy Level Alignment in a THF-Processed Fullerene-Free Organic Solar Cell with 11.3% Efficiency. *Adv. Mater.* 29, 1604241 (2017). <https://doi.org/10.1002/adma.201604241>
- [S10] L. Ye, Y. Xiong, Q. Zhang, S. Li, C. Wang et al., Surpassing 10% Efficiency Benchmark for Nonfullerene Organic Solar Cells by Scalable Coating in Air from Single Nonhalogenated Solvent. *Adv. Mater.* 30, 1705485 (2018). <https://doi.org/10.1002/adma.201705485>
- [S11] X. Xu, T. Yu, Z. Bi, W. Ma, Y. Li, Q. Peng, Realizing Over 13% Efficiency in Green-Solvent-Processed Nonfullerene Organic Solar Cells Enabled by 1,3,4-Thiadiazole-Based Wide-Bandgap Copolymers. *Adv. Mater.* 30, 1703973 (2018) <https://doi.org/10.1002/adma.201703973>
- [S12] W. Zhao, S. Zhang, Y. Zhang, S. Li, X. Liu et al., Environmentally Friendly Solvent-Processed Organic Solar Cells that are Highly Efficient and Adaptable for the Blade-Coating Method. *Adv. Mater.* 30, 1704837 (2018). <https://doi.org/10.1002/adma.201704837>
- [S13] Y. Qin, L. Ye, S. Zhang, J. Zhu, B. Yang et al., A polymer design strategy toward green solvent processed efficient non-fullerene polymer solar cells. *J Mater. Chem. A* 6, 4324-4330 (2018). <https://doi.org/10.1039/C8TA00368H>
- [S14] Q. Fan, Q. Zhu, Z. Xu, W. Su, J. Chen et al., Chlorine substituted 2D-conjugated polymer for high-performance polymer solar cells with 13.1% efficiency via toluene processing. *Nano Energy* 48, 413-420 (2018). <https://doi.org/10.1016/j.nanoen.2018.04.002>
- [S15] X. Cheng, M. Li, Z. Guo, J. Yu, G. Lu et al., "Twisted" conjugated molecules as donor materials for efficient all-small-molecule organic solar cells processed with tetrahydrofuran. *J. Mater. Chem. A* 7, 23008-23018 (2019). <https://doi.org/10.1039/C9TA07760J>
- [S16] U. K. Aryal, S. S. Reddy, K. Kranthiraja, J. Kim, W. Cho et al., Nonhalogenated Solvent-Processed Fullerene-Free Ambient Stable Organic Solar Cells: Impact of Molecular Weight of New π -Conjugated Donor Polymer on Efficiency. *ACS Appl. Energy Mater.* 2, 4159-4166 (2019). <https://doi.org/10.1021/acsaem.9b00365>
- [S17] C. Liao, M. Zhang, X. Xu, F. Liu, Y. Li et al., Green solvent-processed efficient non-fullerene organic solar cells enabled by low-bandgap copolymer donors with

- EDOT side chains. *J. Mater. Chem. A* 7, 716-726 (2019).
<https://doi.org/10.1039/C8TA10882J>
- [S18] Q. Liao, K. Yang, J. Chen, C. W. Koh, Y. Tang et al., (2019). Backbone Coplanarity Tuning of 1,4-Di(3-alkoxy-2-thienyl)-2,5-difluorophenylene-Based Wide Bandgap Polymers for Efficient Organic Solar Cells Processed from Nonhalogenated Solvent. *ACS Appl. Mater. Interfaces* 11, 31119-31128.
<https://doi.org/10.1021/acsmami.9b09692>
- [S19] Y. Tang, H. Sun, Z. Wu, Y. Zhang, G. Zhang et al., A New Wide Bandgap Donor Polymer for Efficient Nonfullerene Organic Solar Cells with a Large Open-Circuit Voltage. *Adv. Sci.* 6, 1901773 (2019).
<https://doi.org/10.1002/advs.201901773>
- [S20] S. Dong, K. Zhang, B. Xie, J. Xiao, H.-L. Yip et al., High-Performance Large-Area Organic Solar Cells Enabled by Sequential Bilayer Processing via Nonhalogenated Solvents. *Adv. Energy Mater.* 9, 1802832 (2019).
<https://doi.org/10.1002/aenm.201802832>
- [S21] S. J. Jeon, Y. W. Han, D. K. Moon, 13.9%-Efficiency and Eco-Friendly Nonfullerene Polymer Solar Cells Obtained by Balancing Molecular Weight and Solubility in Chlorinated Thiophene-Based Polymer Backbones. *Small* 15, 1902598 (2019).
<https://doi.org/10.1002/smll.201902598>
- [S22] J. Chen, G. Li, Q. Zhu, X. Guo, Q. Fan et al., Highly efficient near-infrared and semitransparent polymer solar cells based on an ultra-narrow bandgap nonfullerene acceptor. *J. Mater. Chem. A* 7, 3745-3751 (2019).
<https://doi.org/10.1039/C8TA11484F>
- [S23] Y. Cui, H. Yao, L. Hong, T. Zhang, Y. Xu, et al., Achieving Over 15% Efficiency in Organic Photovoltaic Cells via Copolymer Design. *Adv. Mater.* 31, 1808356 (2019).
<https://doi.org/10.1002/adma.201808356>
- [S24] L. Hong, H. Yao, Z. Wu, Y. Cui, T. Zhang et al., Eco-Compatible Solvent-Processed Organic Photovoltaic Cells with Over 16% Efficiency. *Adv. Mater.* 31, 1903441 (2019). <https://doi.org/10.1002/adma.201903441>
- [S25] R. Sun, T. Wang, Z. Luo, Z. Hu, F. Huang et al. Achieving Eco-Compatible Organic Solar Cells with Efficiency >16.5% Based on an Iridium Complex-Incorporated Polymer Donor. *Sol. RRL* 4, 2000156 (2020). <https://doi.org/10.1002/solr.202000156>
- [S26] S. Dong, T. Jia, K. Zhang, J. Jing, F. Huang, Single-Component Non-halogen Solvent-Processed High-Performance Organic Solar Cell Module with Efficiency over 14%. *Joule* 4, 2004-2016 (2020). <https://doi.org/10.1016/j.joule.2020.07.028>
- [S27] H. Huang, X. Li, C. Sun, I. Angunawela, B. Qiu et al., Green solvent-processed organic solar cells based on a low cost polymer donor and a small molecule acceptor. *J. Mater. Chem. C* 8, 7718-7724 (2020). <https://doi.org/10.1039/D0TC01313G>
- [S28] C.-H. Zhang, F. Lin, W. Huang, J. Xin, J. Wang et al., Methyl functionalization on conjugated side chains for polymer solar cells processed from non-chlorinated solvents. *J. Mater. Chem. C* 8, 11532-11539 (2020). <https://doi.org/10.1039/D0TC02032J>
- [S29] X. Xu, L. Yu, H. Yan, R. Li, Q. Peng, Highly efficient non-fullerene organic solar cells enabled by a delayed processing method using a non-halogenated solvent. *Energy Environ. Sci.* 13, 4381-4388 (2020). <https://doi.org/10.1039/D0EE02034F>
- [S30] B. Fan, F. Lin, J. Oh, H. Fu, W. Gao et al., Enabling High Efficiency of Hydrocarbon-Solvent Processed Organic Solar Cells through Balanced Charge

- Generation and Non-Radiative Loss. *Adv. Energy Mater.* 11, 2101768 (2021).
<https://doi.org/10.1002/aenm.202101768>
- [S31] C. Kim, S. Chen, J. S. Park, G.-U. Kim, H. Kang et al., Green solvent-processed, high-performance organic solar cells achieved by outer side-chain selection of selenophene-incorporated Y-series acceptors. *J. Mater. Chem. A* 9, 24622-24630 (2021). <https://doi.org/10.1039/D1TA07046K>
- [S32] H. Chen, H. Lai, Z. Chen, Y. Zhu, H. Wang et al., 17.1 %-Efficient Eco-Compatible Organic Solar Cells from a Dissymmetric 3D Network Acceptor. *Angew. Chem. Int. Ed.* 60, 3238-3246 (2021).
<https://doi.org/10.1002/anie.202013053>
- [S33] S. Qin, Z. Jia, L. Meng, C. Zhu, W. Lai et al., Non-Halogenated-Solvent Processed and Additive-Free Tandem Organic Solar Cell with Efficiency Reaching 16.67%. *Adv. Funct. Mater.* 31, 2102361 (2021). <https://doi.org/10.1002/adfm.202102361>
- [S34] W. Sun, H. Chen, B. Zhang, Q. Cheng, H. Yang et al., Host-Guest Active Layer Enabling Annealing-Free, Nonhalogenated Green Solvent Processing for High-Performance Organic Solar Cells. *Chin. J. Chem.* 40, 2963-2972 (2022).
<https://doi.org/10.1002/cjoc.202200437>
- [S35] J. Wan, L. Zeng, X. Liao, Z. Chen, S. Liu et al., All-Green Solvent-Processed Planar Heterojunction Organic Solar Cells with Outstanding Power Conversion Efficiency of 16%. *Adv. Funct. Mater.* 32, 2107567 (2022).
<https://doi.org/10.1002/adfm.202107567>
- [S36] J. Zhang, Q. Huang, K. Zhang, T. Jia, J. Jing et al., Random copolymerization strategy for non-halogenated solvent-processed all-polymer solar cells with a high efficiency of over 17%. *Energy Environ. Sci.* 15, 4561-4571 (2022).
<https://doi.org/10.1039/D2EE01996E>
- [S37] K. Hu, C. Zhu, K. Ding, S. Qin, W. Lai et al., Solid additive tuning of polymer blend morphology enables non-halogenated-solvent all-polymer solar cells with an efficiency of over 17%. *Energy Environ. Sci.* 15, 4157-4166 (2022).
<https://doi.org/10.1039/D2EE01727J>
- [S38] J. Wan, Y. Wu, R. Sun, J. Qiao, X. Hao et al., An alloy small molecule acceptor for green printing organic solar cells overcoming the scaling lag of efficiency. *Energy Environ. Sci.* 15, 5192-5201 (2022). <https://doi.org/10.1039/D2EE03134E>
- [S39] H. Xia, Y. Zhang, W. Deng, K. Liu, X. Xia et al. Novel Oligomer Enables Green Solvent Processed 17.5% Ternary Organic Solar Cells: Synergistic Energy Loss Reduction and Morphology Fine-Tuning. *Adv. Mater.* 34, 2107659 (2022).
<https://doi.org/10.1002/adma.202205638>
- [S40] H. Lu, H. Wang, G. Ran, S. Li, J. Zhang et al., Random Terpolymer Enabling High-Efficiency Organic Solar Cells Processed by Nonhalogenated Solvent with a Low Nonradiative Energy Loss. *Adv. Funct. Mater.* 32, 2203193 (2022).
<https://doi.org/10.1002/adfm.202203193>
- [S41] J. Liu, J. Deng, Y. Zhu, X. Geng, L. Zhang et al., Regulation of Polymer Configurations Enables Green Solvent-Processed Large-Area Binary All-Polymer Solar Cells With Breakthrough Performance and High Efficiency Stretchability Factor. *Adv. Mater.* 35, 2208008 (2023). <https://doi.org/10.1002/adma.202208008>
- [S42] S. Pang, Z. Chen, J. Li, Y. Chen, Z. Liu et al., High-efficiency organic solar cells processed from a real green solvent. *Mater. Horiz.* 10, 473-482 (2023).

<https://doi.org/10.1039/D2MH01314B>

- [S43] J. Shi, Z. Chen, Y. Qiu, M. Luo, X. Zhang et al., Facile Side Chains Optimization of Y-series Acceptor Enables High Performance Binary Non-halogenated Solvent-Processed Organic Solar Cells with Excellent Fill Factor of 79%. *Sol. RRL* 7, 2300206 (2023). <https://doi.org/10.1002/solr.202300206>
- [S44] D. Vak, K. Hwang, A. Faulks, Y.-S. Jung, N. Clark et al., 3D Printer Based Slot-Die Coater as a Lab-to-Fab Translation Tool for Solution-Processed Solar Cells. *Adv. Energy Mater.* 5, 1401539 (2015). <https://doi.org/10.1002/aenm.201401539>
- [S45] H. W. Ro, J. M. Downing, S. Engmann, A. A. Herzing, D. M. DeLongchamp et al., Morphology changes upon scaling a high-efficiency, solution-processed solar cell. *Energy Environ. Sci.* 9, 2835-2846 (2016). <https://doi.org/10.1039/C6EE01623E>
- [S46] S. Hong, H. Kang, G. Kim, S. Lee, S. Kim et al., A series connection architecture for large-area organic photovoltaic modules with a 7.5% module efficiency. *Nat. Commun.* 7, 10279 (2016). <https://doi.org/10.1038/ncomms10279>
- [S47] L. Zhang, X. Xu, B. Lin, H. Zhao, T. Li et al., (2018). Achieving Balanced Crystallinity of Donor and Acceptor by Combining Blade-Coating and Ternary Strategies in Organic Solar Cells. *Adv. Mater.* 30, 1805041. <https://doi.org/10.1002/adma.201805041>
- [S48] S. Strohm, F. Machui, S. Langner, P. Kubis, N. Gasparini et al., P3HT: non-fullerene acceptor based large area, semi-transparent PV modules with power conversion efficiencies of 5%, processed by industrially scalable methods. *Energy Environ. Sci.* 11, 2225-2234 (2018). <https://doi.org/10.1039/C8EE01150H>
- [S49] Q. Kang, L. Ye, B. Xu, C. An, S. J. Stuard et al., A Printable Organic Cathode Interlayer Enables over 13% Efficiency for 1-cm² Organic Solar Cells. *Joule* 3, 227-239 (2019). <https://doi.org/10.1016/j.joule.2018.10.024>
- [S50] S. Dong, K. Zhang, T. Jia, W. Zhong, X. Wang et al., Suppressing the excessive aggregation of nonfullerene acceptor in blade-coated active layer by using n-type polymer additive to achieve large-area printed organic solar cells with efficiency over 15%. *EcoMat* 1, e12006 (2019). <https://doi.org/10.1002/eom2.12006>
- [S51] G. Ji, W. Zhao, J. Wei, L. Yan, Y. Han et al., 12.88% efficiency in doctor-blade coated organic solar cells through optimizing the surface morphology of a ZnO cathode buffer layer. *J. Mater. Chem. A* 7, 212-220 (2019). <https://doi.org/10.1039/C8TA08873J>
- [S52] L. Zhang, H. Zhao, B. Lin, J. Yuan, X. Xu et al., A blade-coated highly efficient thick active layer for non-fullerene organic solar cells. *J. Mater. Chem. A* 7, 22265-22273 (2019). <https://doi.org/10.1039/C9TA09799F>
- [S53] Q. Kang, Q. Liao, Y. Xu, L. Xu, Y. Zu et al., p-Doped Conducting Polyelectrolyte as an Anode Interlayer Enables High Efficiency for 1 cm² Printed Organic Solar Cells. *ACS Appl. Mater. Interfaces* 11, 20205-20213 (2019). <https://doi.org/10.1021/acsami.9b04211>
- [S54] S. Rasool, D. V. Vu, C. E. Song, H. K. Lee, S. K. Lee et al., Room Temperature Processed Highly Efficient Large-Area Polymer Solar Cells Achieved with Molecular Engineering of Copolymers. *Adv. Energy Mater.* 9, 1900168 (2019). <https://doi.org/10.1002/aenm.201900168>
- [S55] S.-H. Chen, C. H. Liao, C. Y. Chang, K. M. Huang, J. Y. Chen et al. Large-area blade-coated organic solar cells processed from halogen-free solvent. *Org. Electron.*

75, 105376 (2019). <https://doi.org/10.1016/j.orgel.2019.105376>

- [S56] R. Sun, J. Guo, C. Sun, T. Wang, Z. Luo et al. A universal layer-by-layer solution-processing approach for efficient non-fullerene organic solar cells. *Energy Environ. Sci.* 12, 384-395 (2019). <https://doi.org/10.1039/C8EE02560F>
- [S57] Q. Wu, J. Guo, R. Sun, J. Guo, S. Jia et al., Slot-die printed non-fullerene organic solar cells with the highest efficiency of 12.9% for low-cost PV-driven water splitting. *Nano Energy* 61, 559-566 (2019). <https://doi.org/10.1016/j.nanoen.2019.04.091>
- [S58] R. Sun, J. Guo, Q. Wu, Z. Zhang, W. Yang et al., A multi-objective optimization-based layer-by-layer blade-coating approach for organic solar cells: rational control of vertical stratification for high performance. *Energy Environ. Sci.* 12, 3118-313 (2019). <https://doi.org/10.1039/C9EE02295C>
- [S59] C. Zhu, H. Huang, Z. Jia, F. Cai, J. Li et al., Spin-coated 10.46% and blade-coated 9.52% of ternary semitransparent organic solar cells with 26.56% average visible transmittance. *Sol. Energy* 204, 660-666 (2020).
<https://doi.org/10.1016/j.solener.2020.05.027>
- [S60] X. Han, J. Zhu, Y. Xiao, H. Jiang, Z. Zhang et al., An Alkoxy-Solubilizing Decacyclic Electron Acceptor for Efficient Ecofriendly As-Cast Blade-Coated Organic Solar Cells. *Sol. RRL* 4, 2000108 (2020). <https://doi.org/10.1002/solr.202000108>
- [S61] Y. Cui, H. Yao, L. Hong, T. Zhang, Y. Tang et al., Organic photovoltaic cell with 17% efficiency and superior processability. *Natl. Sci. Rev.* 7, 1239-1246 (2020).
<https://doi.org/10.1093/nsr/nwz200>
- [S62] K. Weng, L. Ye, L. Zhu, J. Xu, J. Zhou et al., Optimized active layer morphology toward efficient and polymer batch insensitive organic solar cells. *Nat. Commun.* 11, 2855 (2020). <https://doi.org/10.1038/s41467-020-16621-x>
- [S63] R. Sun, Q. Wu, J. Guo, T. Wang, Y. Wu et al. A Layer-by-Layer Architecture for Printable Organic Solar Cells Overcoming the Scaling Lag of Module Efficiency. *Joule* 4, 407-419 (2020). <https://doi.org/10.1016/j.joule.2019.12.004>
- [S64] Y. Wang, X. Wang, B. Lin, Z. Bi, X. Zhou et al., Achieving Balanced Crystallization Kinetics of Donor and Acceptor by Sequential-Blade Coated Double Bulk Heterojunction Organic Solar Cells. *Adv. Energy Mater.* 10, 2000826 (2020).
<https://doi.org/10.1002/aenm.202000826>
- [S65] Y. Li, H. Liu, J. Wu, H. Tang, H. Wang et al., Additive and High-Temperature Processing Boost the Photovoltaic Performance of Nonfullerene Organic Solar Cells Fabricated with Blade Coating and Nonhalogenated Solvents. *ACS Appl. Mater. Interfaces* 13, 10239-10248 (2021). <https://doi.org/10.1021/acsami.0c23035>
- [S66] J. Yuan, D. Liu, H. Zhao, B. Lin, X. Zhou et al., Patterned Blade Coating Strategy Enables the Enhanced Device Reproducibility and Optimized Morphology of Organic Solar Cells. *Adv. Energy Mater.* 11, 2100098 (2021).
<https://doi.org/10.1002/aenm.202100098>
- [S67] Y. Zhang, K. Liu, J. Huang, X. Xia, J. Cao et al. Graded bulk-heterojunction enables 17% binary organic solar cells via nonhalogenated open air coating. *Nat. Commun.* 12, 4815 (2021). <https://doi.org/10.1038/s41467-021-25148-8>
- [S68] H. Zhao, B. Lin, J. Xue, H. B. Naveed, C. Zhao et al., (2022). Kinetics Manipulation Enables High-Performance Thick Ternary Organic Solar Cells via R2R-Compatible Slot-Die Coating. *Adv. Mater.* 34, 2105114.
<https://doi.org/10.1002/adma.202105114>

- [S69] Q. Zhu, J. Xue, G. Lu, B. Lin, H. B. Naveed et al., Efficient and mechanically-robust organic solar cells based on vertical stratification modulation through sequential blade-coating. *Nano Energy* 97, 107194 (2022).
<https://doi.org/10.1016/j.nanoen.2022.107194>
- [S70] J. Xue, H. Zhao, B. Lin, Y. Wang, Q. Zhu et al., Nonhalogenated Dual-Slot-Die Processing Enables High-Efficiency Organic Solar Cells. *Adv. Mater.* 34, 2202659 (2022). <https://doi.org/10.1002/adma.202202659>
- [S71] S R. Sun, T. Wang, X. Yang, Y. Wu, Y. Wang et al., High-speed sequential deposition of photoactive layers for organic solar cell manufacturing. *Nat. Energy* 7, 1087-1099 (2022). <https://doi.org/10.1038/s41560-022-01140-4>